The Astrophysical Journal Supplement Series, 282:62 (24pp), 2026 February https://doi.org/10.3847/1538-4365/ae18d3

Dark Energy Survey Year 6 Results: Photometric Dataset for Cosmology

K. Bechtol[1], I. Sevilla-Noarbe[2], A. Drlica-Wagner[3,4,5,6], B. Yanny[3], R. A. Gruendl[7,8], E. Sheldon[9], E. S. Rykoff[10,11], J. De Vicente[2], M. Adamow[7], D. Anbajagane[5], M. R. Becker[12], G. M. Bernstein[13], A. Carnero Rosell[14,15,16], J. Gschwend[15], M. Gorsuch[1], W. G. Hartley[17], M. Jarvis[13], T. Jeltema[18], R. Kron[3,4,5], T. A. Manning[7], J. O'Donnell[3,5,18], A. Pieres[15,19], M. Rodríguez-Monroy[20], D. Sanchez Cid[2], M. Tabbutt[1], C. Y. Tan[4,5], L. Toribio San Cipriano[2], D. L. Tucker[3], N. Weaverdyck[21,22], M. Yamamoto[23,24], T. M. C. Abbott[25], M. Aguena[15], A. Alarcón[26], S. Allam[3], A. Amon[23], F. Andrade-Oliveira[27], S. Avila[2], P. H. Bernardinelli[28], E. Bertin[29,30], J. Blazek[31], D. Brooks[32], D. L. Burke[10,11], J. Carretero[33], F. J. Castander[26,34], R. Cawthon[35], C. Chang[4,5], A. Choi[36], C. Conselice[37,38], M. Costanzi[39,40,41], M. Crocce[34,26], L. N. da Costa[15], T. M. Davis[42], S. Desai[43], H. T. Diehl[3], S. Dodelson[3,4,5], P. Doel[32], C. Doux[13,44], A. Ferté[11], B. Flaugher[3], P. Fosalba[26,34], J. Frieman[3,4,5], J. García-Bellido[20], M. Gatti[5,13], E. Gaztanaga[26,34,45], G. Giannini[5,33], D. Gruen[46], G. Gutierrez[3], K. Herner[3], S. R. Hinton[42], D. L. Hollowood[18], K. Honscheid[47,48], D. Huterer[49], N. Jeffrey[32], E. Krause[50], K. Kuehn[51,52], O. Lahav[32], S. Lee[53], C. Lidman[54,55], M. Lima[15,56], H. Lin[3], J. L. Marshall[57], J. Mena-Fernández[58], R. Miquel[33,59], J. J. Mohr[46,60], J. Muir[61], J. Myles[23], R. L. C. Ogando[19], A. Palmese[62], A. A. Plazas Malagón[10,11], A. Porredon[2,63], J. Prat[4,64], M. Raveri[65], A. K. Romer[66], A. Roodman[10,11], S. Samuroff[31,33], E. Sanchez[2], V. Scarpine[3], M. Smith[67], M. Soares-Santos[27], E. Suchyta[68], G. Tarle[49], M. A. Troxel[24], V. Vikram[12], A. R. Walker[25], J. Weller[60,69], P. Wiseman[70], and Y. Zhang[71]

(DES Collaboration)

[1] Physics Department, 2320 Chamberlin Hall, University of Wisconsin-Madison, 1150 University Avenue Madison, WI 53706-1390, USA; kbechtol@wisc.edu
[2] Centro de Investigaciones Energéticas, Medioambientales y Tecnológicas (CIEMAT), Madrid, Spain; ignacio.sevilla@ciemat.es
[3] Fermi National Accelerator Laboratory, P. O. Box 500, Batavia, IL 60510, USA; kadrlica@fnal.gov
[4] Department of Astronomy and Astrophysics, University of Chicago, Chicago, IL 60637, USA
[5] Kavli Institute for Cosmological Physics, University of Chicago, Chicago, IL 60637, USA
[6] NSF-Simons AI Institute for the Sky (SkAI), 172 E. Chestnut Street, Chicago, IL 60611, USA
[7] Center for Astrophysical Surveys, National Center for Supercomputing Applications, 1205 West Clark Street, Urbana, IL 61801, USA
[8] Department of Astronomy, University of Illinois at Urbana-Champaign, 1002 W. Green Street, Urbana, IL 61801, USA
[9] Brookhaven National Laboratory, Bldg 510, Upton, NY 11973, USA
[10] Kavli Institute for Particle Astrophysics & Cosmology, P. O. Box 2450, Stanford University, Stanford, CA 94305, USA
[11] SLAC National Accelerator Laboratory, Menlo Park, CA 94025, USA
[12] Argonne National Laboratory, 9700 South Cass Avenue, Lemont, IL 60439, USA
[13] Department of Physics and Astronomy, University of Pennsylvania, Philadelphia, PA 19104, USA
[14] Instituto de Astrofisica de Canarias, E-38205 La Laguna, Tenerife, Spain
[15] Laboratório Interinstitucional de e-Astronomia - LIneA, Rua Gal. José Cristino 77, Rio de Janeiro, RJ 20921-400, Brazil
[16] Universidad de La Laguna, Dpto. Astrofísica, E-38206 La Laguna, Tenerife, Spain
[17] Department of Astronomy, University of Geneva, ch. d'Écogia 16, CH-1290 Versoix, Switzerland
[18] Santa Cruz Institute for Particle Physics, Santa Cruz, CA 95064, USA
[19] Observatório Nacional, Rua Gal. José Cristino 77, Rio de Janeiro, RJ 20921-400, Brazil
[20] Instituto de Fisica Teorica UAM/CSIC, Universidad Autonoma de Madrid, 28049 Madrid, Spain
[21] Department of Astronomy, University of California, Berkeley, 501 Campbell Hall, Berkeley, CA 94720, USA
[22] Lawrence Berkeley National Laboratory, 1 Cyclotron Road, Berkeley, CA 94720, USA
[23] Department of Astrophysical Sciences, Princeton University, Peyton Hall, Princeton, NJ 08544, USA
[24] Department of Physics, Duke University, Durham, NC 27708, USA
[25] Cerro Tololo Inter-American Observatory/NSF NOIRLab, Casilla 603, La Serena, Chile
[26] Institute of Space Sciences (ICE, CSIC), Campus UAB, Carrer de Can Magrans, s/n, 08193 Barcelona, Spain
[27] Physik-Institut—University of Zurich, Winterthurerstrasse 190, 8057 Zurich, Switzerland
[28] Astronomy Department, University of Washington, Box 351580, Seattle, WA 98195, USA
[29] CNRS, UMR 7095, Institut d'Astrophysique de Paris, F-75014, Paris, France
[30] Sorbonne Universités, UPMC Univ Paris 06, UMR 7095, Institut d'Astrophysique de Paris, F-75014, Paris, France
[31] Department of Physics, Northeastern University, Boston, MA 02115, USA
[32] Department of Physics & Astronomy, University College London, Gower Street, London, WC1E 6BT, UK
[33] Institut de Física d'Altes Energies (IFAE), The Barcelona Institute of Science and Technology, Campus UAB, 08193 Bellaterra (Barcelona), Spain
[34] Institut d'Estudis Espacials de Catalunya (IEEC), 08034 Barcelona, Spain
[35] Physics Department, William Jewell College, Liberty, MO 64068, USA
[36] NASA Goddard Space Flight Center, 8800 Greenbelt Road, Greenbelt, MD 20771, USA
[37] Jodrell Bank Center for Astrophysics, School of Physics and Astronomy, University of Manchester, Oxford Road, Manchester, M13 9PL, UK
[38] University of Nottingham, School of Physics and Astronomy, Nottingham NG7 2RD, UK
[39] Astronomy Unit, Department of Physics, University of Trieste, via Tiepolo 11, I-34131 Trieste, Italy
[40] INAF-Osservatorio Astronomico di Trieste, via G. B. Tiepolo 11, I-34143 Trieste, Italy
[41] Institute for Fundamental Physics of the Universe, Via Beirut 2, 34014 Trieste, Italy
[42] School of Mathematics and Physics, University of Queensland, Brisbane, QLD 4072, Australia
[43] Department of Physics, IIT Hyderabad, Kandi, Telangana 502285, India
[44] Université Grenoble Alpes, CNRS, LPSC-IN2P3, 38000 Grenoble, France
[45] Institute of Cosmology and Gravitation, University of Portsmouth, Portsmouth, PO1 3FX, UK
[46] University Observatory, Faculty of Physics, Ludwig-Maximilians-Universität, Scheinerstr. 1, 81679 Munich, Germany
[47] Center for Cosmology and Astro-Particle Physics, The Ohio State University, Columbus, OH 43210, USA
[48] Department of Physics, The Ohio State University, Columbus, OH 43210, USA

[49] Department of Physics, University of Michigan, Ann Arbor, MI 48109, USA
[50] Department of Astronomy/Steward Observatory, University of Arizona, 933 North Cherry Avenue, Tucson, AZ 85721-0065, USA
[51] Australian Astronomical Optics, Macquarie University, North Ryde, NSW 2113, Australia
[52] Lowell Observatory, 1400 Mars Hill Road, Flagstaff, AZ 86001, USA
[53] Jet Propulsion Laboratory, California Institute of Technology, 4800 Oak Grove Drive, Pasadena, CA 91109, USA
[54] Centre for Gravitational Astrophysics, College of Science, The Australian National University, ACT 2601, Australia
[55] The Research School of Astronomy and Astrophysics, Australian National University, ACT 2601, Australia
[56] Departamento de Física Matemática, Instituto de Física, Universidade de São Paulo, CP 66318, São Paulo, SP 05314-970, Brazil
[57] George P. and Cynthia Woods Mitchell Institute for Fundamental Physics and Astronomy, and Department of Physics and Astronomy, Texas A&M University, College Station, TX 77843, USA
[58] LPSC Grenoble-53, Avenue des Martyrs 38026 Grenoble, France
[59] Institució Catalana de Recerca i Estudis Avançats, E-08010 Barcelona, Spain
[60] Max Planck Institute for Extraterrestrial Physics, Giessenbachstrasse, 85748 Garching, Germany
[61] Perimeter Institute for Theoretical Physics, 31 Caroline Street North, Waterloo, ON N2L 2Y5, Canada
[62] Department of Physics, Carnegie Mellon University, Pittsburgh, PA 15312, USA
[63] Ruhr University Bochum, Faculty of Physics and Astronomy, Astronomical Institute, German Centre for Cosmological Lensing, 44780 Bochum, Germany
[64] Nordita, KTH Royal Institute of Technology and Stockholm University, Hannes Alfvéns väg 12, SE-10691 Stockholm, Sweden
[65] Department of Physics, University of Genova and INFN, Via Dodecaneso 33, 16146, Genova, Italy
[66] Department of Physics and Astronomy, Pevensey Building, University of Sussex, Brighton, BN1 9QH, UK
[67] Physics Department, Lancaster University, Lancaster, LA1 4YB, UK
[68] Computer Science and Mathematics Division, Oak Ridge National Laboratory, Oak Ridge, TN 37831, USA
[69] Universitäts-Sternwarte, Fakultät für Physik, Ludwig-Maximilians Universität München, Scheinerstr. 1, 81679 München, Germany
[70] School of Physics and Astronomy, University of Southampton, Southampton, SO17 1BJ, UK
[71] Community Science and Data Center/NSF NOIRLab, 950 N. Cherry Avenue, Tucson, AZ 85719, USA

Received 2025 May 8; revised 2025 October 27; accepted 2025 October 27; published 2026 February 2

Abstract

We describe the photometric dataset assembled from the full 6 yr of observations by the Dark Energy Survey (DES) in support of static-sky cosmology analyses. DES Y6 Gold is a curated dataset derived from DES Data Release 2 (DR2) that incorporates improved measurement, photometric calibration, object classification and value-added information. Y6 Gold comprises nearly 5000 deg^2 of $grizY$ imaging in the south Galactic cap and includes 669 million objects with a depth of $i_{AB} \sim 23.4$ mag at a signal-to-noise ratio ~ 10 for extended objects and a top-of-the-atmosphere photometric uniformity <2 mmag. Y6 Gold augments DES DR2 with simultaneous fits to multiepoch photometry for more robust galaxy shapes, colors, and photometric redshift estimates. Y6 Gold features improved morphological star–galaxy classification with an efficiency of 98.6% and a contamination of 0.8% for galaxies with $17.5 < i_{AB} < 22.5$. Additionally, it includes per-object quality information, and accompanying maps of the footprint coverage, masked regions, imaging depth, survey conditions, and astrophysical foregrounds that are used for cosmology analyses. After quality selections, benchmark samples contain 448 million galaxies and 120 million stars. This publication is complemented by data access and documentation.

Unified Astronomy Thesaurus concepts: Sky surveys (1464); Observational cosmology (1146); Dark energy (351); Astronomy image processing (2306); Catalogs (205)

1. Introduction

Optical and near-infrared imaging surveys have played an essential role in developing the standard model of cosmology that invokes a cosmological constant and cold, collisionless dark matter (ΛCDM). For a fixed allocation of telescope observing time, broadband photometric surveys assemble the largest samples of galaxies that can be used for statistical analyses, while also providing the opportunity to combine several complementary probes of the cosmic expansion history and growth of structure (e.g., T. M. C. Abbott et al. 2019; C. Heymans et al. 2021). The current generation of imaging surveys, such as the Pan-STARRS1 surveys (K. C. Chambers et al. 2016), the Hyper Suprime-Cam Subaru Strategic Program (HSC-SSP; H. Aihara et al. 2019), the Ultraviolet Near-Infrared Optical Northern Survey (S. Gwyn et al. 2025), the Kilo-Degree Survey (K. Kuijken et al. 2019), the DESI Legacy Imaging Surveys (A. Dey et al. 2019), the Dark Energy Camera (DECam) Local Volume Exploration survey (A. Drlica-Wagner et al. 2021), and the Dark Energy Survey (DES; DES Collaboration 2005, 2016) collectively provide deep, multiband imaging over nearly the entire high-Galactic-latitude sky, and have cataloged more than a billion galaxies and thousands of supernovae spanning 10 Gyr of cosmic history. Together with spectroscopic surveys like eBOSS (S. Alam et al. 2021) and DESI (DESI Collaboration 2016), imaging surveys yield measurements of the expansion rate and large-scale structure in the late-time Universe that are complementary to precision measurements of the early Universe (e.g., Planck Collaboration 2020). Combined analyses of the early- and late-time observations rigorously test the ΛCDM paradigm, with percent-level measurement uncertainties on the ΛCDM model parameters (e.g., DES Collaboration 2022, 2024b, 2024c).

To support both cosmological and other astronomical investigations, DES data products are publicly released via two pathways, as summarized in Table 1. Two general DES data releases, DES DR1 (DES Collaboration 2018) and DES DR2 (DES Collaboration 2021) provide coadded images and associated object catalogs for the first 3 yr and 6 yr of the survey, respectively. Further image-processing algorithms, survey characterization, and value-added data products have

Table 1
Dark Energy Survey Data Releases

Release	Area (sq. deg.)	Depth (i band)	Objects	Photometry Uniformity (mmag)	Supplemental Data	References
SVA1 Gold	~250	23.68	25M	<15	Photo-z	...
Y1 Gold	1786	23.29	137M	<15	BPZ/DNF photo-z, MOF, maps, classification	A. Drlica-Wagner et al. (2018)
DES DR1	5186	23.33	399M	<3	None	DES Collaboration (2018)
Y3 Gold	4946	23.34	388M	<3	BPZ/DNF photo-z, SOF/MOF, maps, classification	I. Sevilla-Noarbe et al. (2021)
Y3 Deep Fields	5.88	25.0	2.8M (1.6M NIR)	<5	*ugrizYJHK* bands	W. G. Hartley et al. 2022
DES DR2	4913	23.8	691M	~2	None	DES Collaboration (2021)
Y6 Gold	4923	23.8	669M	<2	DNF photo-z, `fitvd/GAp`, maps, classification	This work

Note. All releases are publicly accessible at https://des.ncsa.illinois.edu/releases. Quoted depth corresponds to signal-to-noise ratio (S/N) = 10 in 2″ diameter apertures. "SOF" and "MOF" are multiepoch pipelines replaced by `fitvd`, described in Section 3.4. The Y6 Gold area is computed for simultaneous two-exposure coverage in *griz*, whereas the DES DR2 area is quoted for one exposure in all five *grizY* bands.

Table 2
Key Numbers and Data Quality Summary for the DES Wide Survey (Y6 Gold; This Work)

Parameter	Band				
	g	r	i	z	Y
Wide Survey (This Work)					
Median PSF FWHM (arcsec)	1.13	0.99	0.90	0.87	0.93
Sky Coverage (*griz* intersection, deg^2)	4923				
Coadd Median Astrometric Relative Precision (angular distance, mas)	27				
Photometric Uniformity versus Gaia (mmag) [a]	1.8				⋯
Median Coadd Magnitude Limit, 1.″95 diameter (S/N = 10)	24.7	24.4	23.8	23.1	21.7
Coadd 90% Completeness Limit for Extended Objects (mag) [b]	23.9	23.2	22.7	22.4	⋯
Multiepoch Galaxy Magnitude Limit (S/N = 10, BDF) [c]	$24.2^{+0.1}_{-0.2}$	$23.9^{+0.1}_{-0.2}$	$23.4^{+0.1}_{-0.2}$	$22.7^{+0.1}_{-0.2}$	$21.3^{+0.2}_{-0.2}$
Galaxy Selection ($17.5 \leqslant$ `MAG_AUTO_I[i]` $\leqslant 22.5$; `ext_mash` $= 4$)	Efficiency 98.6%; Contamination 0.8%				
Stellar Selection ($17.5 \leqslant$ `MAG_AUTO_I[i]` $\leqslant 22.5$; $0 \leqslant$ `ext_mash` $\leqslant 1$)	Efficiency 94.6%; Contamination 1.5%				
Object density (arcmin^{-2}) [d]	Overall: 37.4; Galaxies: 28.9				

Notes. All magnitudes are in the *AB* system.

[a] Photometric uniformity measured versus Gaia's G band, which encompasses DECam's *griz*.

[b] As measured by BALROG (D. Anbajagane et al. 2025).

[c] Median values with 16% and 84% percentile errors from the magnitude limit distribution.

[d] Object density determined for all objects in Y6 Gold footprint outside foreground regions, and the subset of those classified as high-confidence galaxies (`sof_mash` >= 3).

been developed to control systematic uncertainties at the level required for static-sky cosmology analyses by the DES Collaboration. These data products and validation analyses have been compiled into DES "Gold" releases, including SVA1 Gold, Y1 Gold (A. Drlica-Wagner et al. 2018), and Y3 Gold (I. Sevilla-Noarbe et al. 2021). Here, we present the final iteration of the DES Gold data products, the Year 6 (Y6) Gold, assembled from the full 6 yr DES dataset and intended to support legacy cosmology analyses using the DES data.

DES Y6 Gold is based on the same DECam data that were released as DES DR2. As expected, Y6 Gold is very similar in depth and extent to DR2, but provides additional photometry measurements from multiepoch fitting, photometric redshift estimates, footprint and foreground masks, additional summary flags, survey property maps, and an improved object classification scheme. These products are described in the sections that follow, and Table 2 summarizes a set of metrics that describe the DES Y6 Gold release.

The structure of the paper is as follows. In Section 2, we provide an overview of DES and the resultant 6 yr dataset. Section 3 provides a brief summary of the DES data processing with a focus on new algorithms implemented for Y6 Gold. The value-added content of the Y6 Gold catalog is described in Section 4, whereas the new ancillary maps are detailed in Section 5. We remark on known issues in Section 6 and mechanisms for using the data in Section 7. We conclude by discussing the importance of Y6 Gold in Section 8.

DES Y6 Gold data products and documentation are publicly available at https://des.ncsa.illinois.edu/releases.

2. Survey Overview and Derived Datasets

2.1. Survey Overview

DES used the 570 megapixel Dark Energy Camera (DECam; B. Flaugher et al. 2015) on the 4 m Blanco Telescope at Cerro Tololo Inter-American Observatory in

Chile to image the southern Galactic cap in five broadband filters (*grizY*) extending from ∼400 nm to ∼1060 nm (DES Collaboration 2021). Images were collected on 760 distinct full or half nights between 2013 August 15 and 2019 January 9. DES operated in two survey modes (E. H. Neilsen et al. 2019):

1. The Wide-Field Survey is optimized for cosmological analyses using weak gravitational lensing, galaxy clustering, and galaxy clusters. The Wide-Field Survey spans ∼5000 $\deg^2$ that was imaged with dithered tilings in *grizY* (see DES Collaboration 2021 for details). The Wide-Field Survey footprint was designed to significantly overlap with the South Pole Telescope survey (J. E. Carlstrom et al. 2011) and the Sloan Digital Sky Survey (SDSS) Stripe 82 (K. N. Abazajian et al. 2009), and it includes a connection region to enhance overall calibration. The Wide-Field Survey constitutes the basis for the Y6 Gold dataset.
2. The Supernova Survey is a time-domain survey of 10 DECam fields, amounting to a total of ∼27 $\deg^2$ that was imaged in *griz* with an approximately weekly cadence (M. Smith et al. 2020) with minimal dithering imaging. Difference imaging analysis of the Supernovae Survey fields has enabled the discovery of thousands of Type Ia supernovae (SN Ia), and precision photometric light-curves are computed following D. Brout et al. (2019).

2.2. Derived Datasets

The DES Collaboration has assembled several high-level data products derived from DECam imaging collected by DES:

1. DES DR2 and Y6 Gold are assembled from data collected by the Wide-Field Survey. A total of 76,217 DECam exposures were deemed of sufficient quality to pass onto the next step of image detrending, calibration, and finally coaddition and object detection. DES DR2 and Y6 Gold contain the same number of objects, which were detected and measured by a pipeline based on the `SExtractor` (E. Bertin & S. Arnouts 1996) software (see Section 3 and DES Collaboration 2021 for details). Additional pipelines are run over the DES DR2 coadded catalogs to obtain the Y6 Gold dataset, which are the focus of this paper. The Y6 Gold catalog caters to several science cases including extragalactic astronomy, galaxy cluster cosmology, and cosmology analyses using the large-scale distribution of the positions of the objects according to their photometric properties.
2. The shear catalogs are specialized datasets used for applications that involve weak gravitational lensing measurements. In Year 6, two different shear catalogs were produced using data from the Wide-Field Survey: the Bayesian Fourier Domain method (`BFD`; G. M. Bernstein & R. Armstrong 2014) catalog uses the same detections as DR2 and Y6 Gold, whereas the `metadetect` (E. S. Sheldon et al. 2023) pipeline produces a set of five distinct catalogs based on the same images, which are coadded in a parallel pipeline (M. Yamamoto et al. 2025) and have five different sets of detections. The `metadetect` catalogs are produced to calibrate bias in shear measurements produced by noise, modeling errors, and selection (including detection), as described in E. S. Sheldon et al. (2023). The shear catalogs will be released separately.
3. Finally, the Supernova Survey exposures are coadded to produce the Deep Field datasets. Together with DECam imaging of the COSMOS field,[72] this specialized processing enables high-signal-to-noise-ratio (S/N) measurements of galaxies ∼1.5–2.0 mag fainter than the Wide-Field Survey. A subset of these data have been combined with deep near-infrared imaging to produce a reference object catalog used for various applications in DES cosmology analyses (W. G. Hartley et al. 2022, L. Toribio San Cipriano et al. 2024). A larger region of DECam and NIR deep fields is being processed and analyzed (R. Gruendl et al. 2026, in preparation).

Figure 1 shows the DES footprint, including the Wide-Field Survey and Supernovae Survey. Given the cosmological goals of the survey, DES avoids the Galactic plane to minimize stellar foregrounds and extinction from interstellar dust.

In this work, all quoted data quality characteristics (e.g., Table 2) refer to the subset of exposures included in the DES DR2 coadded images unless stated otherwise.

2.3. Comparison to Y3 Gold

Given the emphasis on the use of Y6 Gold for cosmology measurements, it is worth highlighting improvements over the previous cosmology release, Y3 Gold:

1. Greater depth and uniformity (as shown in Table 1) so that 70% more objects were detected with respect to the previous release.
2. Improved photometry as a consequence of the above.
3. Better point photometric redshift precision (∼20% improvement) and accuracy at $z \sim 1$.
4. A more robust star–galaxy classification, that includes an additional purity level for galaxy samples, as well as a new boosted decision-tree-based algorithm that improves the performance over a larger range of magnitudes.
5. Additional flagging of foreground objects and artifacts.
6. Footprint and foreground maps with higher resolution, and a new map to correct for Galactic cirrus.

3. Data Processing

The DES Data Management system (DESDM; E. Morganson et al. 2018), running at the National Center for Supercomputer Applications (NCSA) as the core data processing center, converted raw DECam data to detrended and coadded images and catalogs. These data were distributed to the DES Collaboration in the form of files and database tables. Additional value-added columns and ancillary data products were produced across several of the collaborating DES institutions and collected at NCSA for distribution.

3.1. Detrending

The single-exposure (or "single-epoch") detrending of instrumental signatures for DES DR1 is described in E. Morganson et al. (2018). The main processing changes implemented for DES

---

[72] http://cosmos.astro.caltech.edu

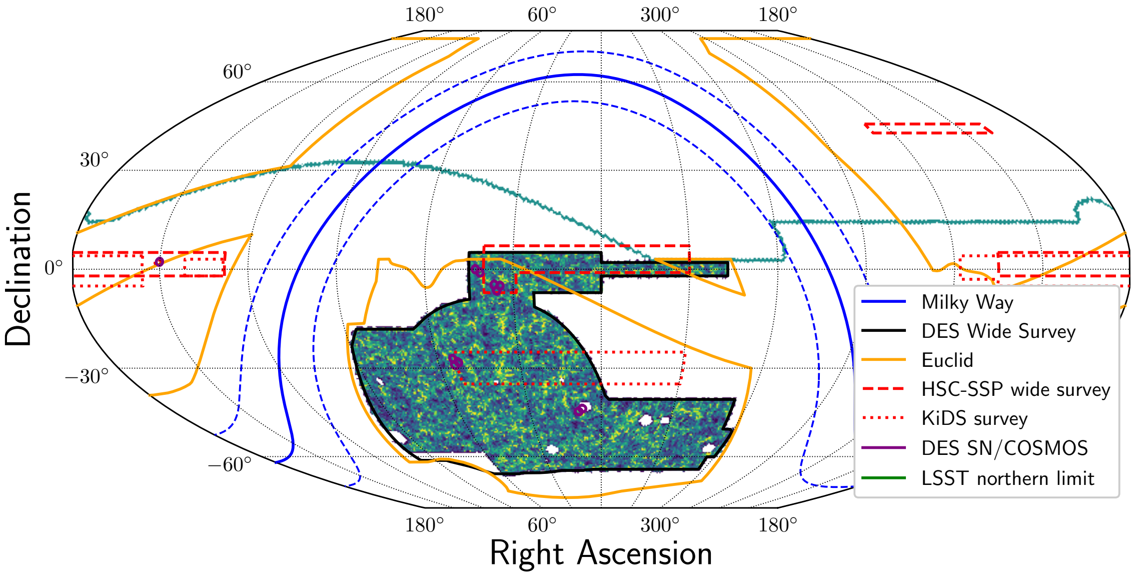

Figure 1. DES footprint in equatorial coordinates. The ∼5000 deg^2 wide-area survey footprint is shown as a black outline, with overplotted REDMAGIC (E. Rozo et al. 2016) galaxies, for the redshift bin $z = [0.5, 0.6]$. The supernova field locations are also shown as purple circles with their approximate area to scale (corresponding to one full DECam field of view). A few other footprints from present and future major photometric surveys are shown for reference. This and the other skymap plots included in this work use the equal-area McBryde–Thomas flat-polar quartic projection (F. W. McBryde & P. Thomas 1949).

DR2 (and shared by Y6 Gold) are described in DES Collaboration (2021) and summarized here:

1. New calibrations (biases, darks, flats, etc.) were derived for the later survey years (Section 3.2).
2. The astrometric reference catalog was updated to Gaia DR2 (Gaia Collaboration 2016, 2018).
3. A utility was introduced to search for and mask a region of anomalous charge arising from a variable hot pixel (“light bulb”) on CCD 46, which was first noticed in exposures shortly after 2017 September 1.
4. A utility was implemented to search for and mask occurrences of an amplifier instability that arose for amplifier *B* of CCD 41 starting 2018 August 15. The instability manifests intermittently as a charge transfer inefficiency that results in streaked row reads with varying background charge. The utility looks for images where the amplifier background is discontinuous from one row to the next and flags the entire amplifier when triggered.[73]
5. A utility was added to use the detections of streaks on individual CCDs (such as those created by satellites) to identify potential trails on adjacent CCDs.
6. The single-epoch catalog effective detection threshold was lowered to $S/N \gtrsim 3$ due to configuration changes in `PSFEx` (E. Bertin 2011), as well as changes to the detection threshold and deblending settings for the initial `SExtractor`-generated catalogs.
7. The sky subtraction algorithm, described in E. Morganson et al. (2018), remains unchanged from Y3: a simultaneous fit to all 60 or 61 CCDs of an exposure with a low-order principal component analysis template is performed to remove large-scale scattered light gradients and a pupil ghost. During image coaddition, a constant median background level is subtracted from each CCD to bring the sky level close to zero.

3.2. Calibration

Y6 Gold measurements build upon the astrometric and photometric calibration of DR2. Thus, the underlying Y6 Gold astrometric positions, tied to Gaia DR2 (Gaia Collaboration 2016, 2018), and photometric calibrations, derived by the forward global calibration module (FGCM; D. L. Burke et al. 2018), are the same as those provided in the DR2 public data release.

The median astrometric precision of the coadd averaged over the DES footprint is estimated to be 27 mas (DES Collaboration 2021). Based on a comparison between Gaia G-band synthesized magnitudes transformed from stellar DES $griz$ magnitudes ($G_{\rm pred}$) and measured Gaia G-band magnitudes ($G_{\rm meas}$) from Gaia DR3 (Gaia Collaboration 2023), the photometric uniformity of Y6 Gold is at the 1.8 mmag (0.18%) rms level or better across the DES footprint (E. S. Rykoff et al. 2023). The absolute calibration of the catalog is computed with reference to the Hubble Space Telescope CalSpec standard star C26202. Including systematic errors, the absolute flux system is known at the ≈1% level. E. S. Rykoff et al. (2023) presented DES $grizY$ magnitudes for 17 million stars with i-band magnitudes mostly in the range $16 \lesssim i \lesssim 21$ as a photometric calibration reference catalog for optical imaging in the southern hemisphere.

All photometry for Y6 Gold is based on the `APER8` system used for FGCM, with aperture corrections computed as described in Section 4.1.1. Briefly, the `APER8` system normalizes point-spread function (PSF)-fitted stellar photometry to aperture photometry within a fixed radius (the eighth in a set of 12 apertures) of diameter $5\farcs84$.

In Figure 2, a qualitative illustration of the improvement of the stellar locus in the vicinity of the globular cluster NGC 1261 is shown in successive Gold releases. The tightness

---

[73] These utilities are publicly available among the DESDM software repositories at https://github.com/DarkEnergySurvey/pixcorrect/.

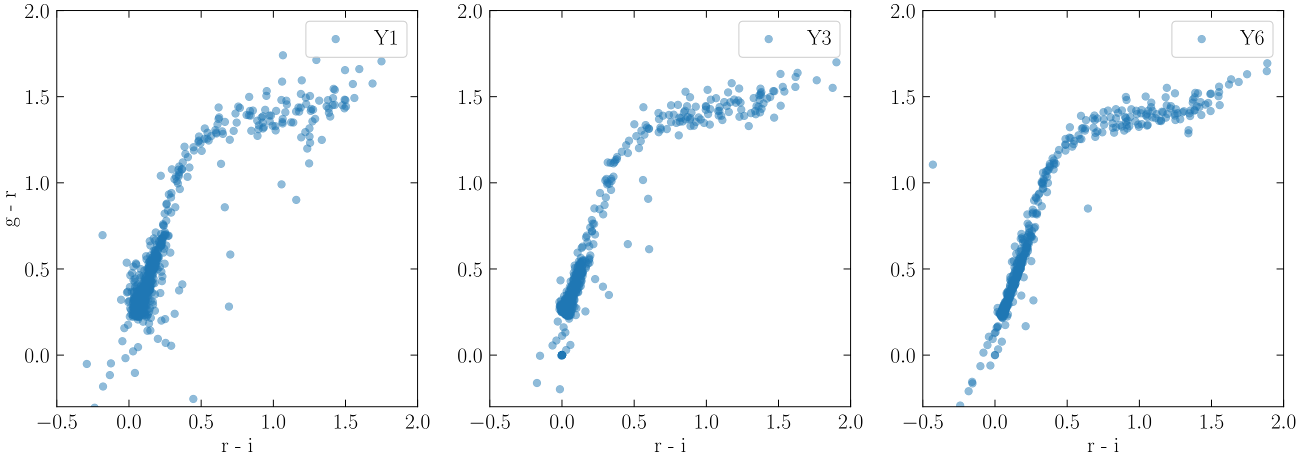

Figure 2. Illustration of the increasing calibration and selection quality in successive data releases, from Y1 Gold (left), Y3 Gold (center), to Y6 Gold (right). This figure shows the stellar locus for selected stars in the outskirts of the globular cluster NGC 1261.

of the stellar locus is indicative of the superior photometric quality in Y6.

3.3. Coaddition and Object Detection

Object detection is performed on combined $r + i + z$ coadd detection images (the three bands simultaneously) using `SExtractor` with an approximate threshold of $S/N \gtrsim 5$, resulting in a set of 691,483,608 objects across the survey footprint, identical to that released in DES DR2. For the DES Y6 cosmological analyses, we run additional forced photometry measurement pipelines starting from this initial detection catalog and compile the results in Y6 Gold.

To facilitate multiepoch photometry, we use the DR2 catalog to build multiepoch data structures (MEDS; M. Jarvis et al. 2016) composed of "postage stamp" images extracted from the coadd and single-epoch images for each object. Along with the science frame data, the postage stamps also carry the weight, mask, background, and PSF model information. Two types of MEDS files were created for Y6. The first set carries single-epoch PSF models from `PSFEx`, and was used for the Y6 Gold photometry measurements using `fitvd` (see Section 3.4). The second set incorporates PSF models generated by `PIFF` (M. Jarvis et al. 2021), and was used with the `BFD` shear measurement pipeline. The other shear pipeline, `metadetect`, also uses `PIFF` PSF models, but uses cell-based coadds rather than MEDS files (E. S. Sheldon et al. 2020).

3.4. Multiepoch Photometry

Similar to previous DES Gold releases, we perform a multiepoch, multiband fit for each object by simultaneously fitting a model to each single-epoch image using the PSF associated with that image. The DES Y1 and Y3 Gold science pipelines performed a multiobject fit (MOF) for each object, where objects were grouped according to a friends-of-friends algorithm (A. Drlica-Wagner et al. 2018; I. Sevilla-Noarbe et al. 2021). A single-object-fit (SOF) variant was also employed that masked nearby objects rather than performing a simultaneous multiobject fit. For DES Y6, object deblending was first performed on coadded images using a new code (`shredder`; see W. G. Hartley et al. 2022). A multiband, multiepoch fit was then performed on the original single-epoch images, with neighbors subtracted using the models from the deblender. The new framework, `fitvd` (first described in W. G. Hartley et al. 2022) performed the neighbor subtraction and ran fitting algorithms from `ngmix` (E. S. Sheldon 2014), using postage stamp images stored in MEDS files. Again, a simpler version using only masking of neighbors was also performed. Ultimately we used only the version with masked neighbors for most analyses, because the photometry was quite consistent for the two techniques. Our interpretation is that blending is not a significant effect on photometry for most objects in the DES data, which is significantly shallower than that of HSC-SSP and the forthcoming Rubin Observatory's Legacy Survey of Space and Time (LSST).

With `fitvd`, we derived object properties using two different algorithms. The first was a PSF template flux measurement, and the second was a galaxy model fit.

For the PSF flux, we used the PSF model from each single-epoch image as a template to extract a single flux constrained by all input images. This flux is linear in the data and is thus highly robust. The PSF flux was determined separately in each band.

The galaxy model profile is a bulge + disk with fixed size ratio (`BDF`). In this model, the fraction of the flux assigned to the bulge and disk components is allowed to vary, but the ratio of bulge size, $T_{\rm bulge}$, to disk size, $T_{\rm disk}$, is fixed to unity (see below for the definition of T). The bulge and disk are further constrained to have the same ellipticity and centroid. Bright, well-resolved galaxies would be better described by a full, flexible bulge+disk model, but both the size ratio and flux ratio would be highly degenerate for faint objects. Fixing the size ratio is a compromise: it reduces the number of degenerate parameters, stabilizes the fit for faint objects, and provides enough flexibility to describe moderately well-resolved galaxies.

The DES Y6 `BDF` model is fit with the following free parameters:

1. The offset from the fiducial position in arcseconds.
2. The flux in each band.
3. The total size squared ($T = \langle x^2 \rangle + \langle y^2 \rangle$) of the full model.
4. The two-component ellipticity (`{g1, g2}`).
5. The fraction of the flux in a bulge (DeVaucouleurs Sérsic model with index $n = 4$), with the remaining flux assigned to an exponential disk (Sérsic model with index $n = 1$).

As mentioned above, the flux ratio is poorly constrained for faint galaxies. To ensure stability, we applied Gaussian prior on with mean 0.5 and $\sigma = 0.1$. We also applied a broad Gaussian prior on the position, with mean equal to the nominal position and σ of 1 pixel, to prevent the model from wandering for very faint objects. We used flat priors for all other parameters.

To fit the model to images from all available epochs and bands, we must first convolve the model by the local PSF and construct a χ^2 between model and data. We fit the reconstructed `PSFEx` image from each epoch to a five-Gaussian model, with all parameters free. The galaxy model was then convolved by this PSF and used to construct a χ^2. The total χ^2 was then calculated by summing the individual χ^2 from all images and bands. Because the model is convolved by the PSF, the derived parameters are "pre-PSF" quantities. Fits to stars have fit sizes close to zero, and star ellipticities are prior-dominated.

The Y6 Gold catalog includes measured fluxes, magnitudes, and uncertainties for the PSF and `BDF` models calculated in each of the individual *grizY* bands. For the `BDF` model, we include the color covariance terms corresponding to each of the off-diagonal elements in the variance matrix of *grizY* photometry. In addition, the Y6 Gold catalog includes the positional offset, size, ellipticity, and `frac_dev`, along with their associated uncertainties, from the `BDF` model fit.

In addition to PSF and `BDF` models, Gaussian aperture (`GAp`) fluxes are also calculated (S. Everett et al. 2022; W. G. Hartley et al. 2022). A Gaussian with FWHM = 4″ is multiplied with the `BDF` model and integrated analytically to give a total flux. While this will necessarily undercount the flux, it is less sensitive to the wings of the object model. This is useful when the `frac_dev` of the object is very noisy, which can result in very noisy total flux estimates. Artificially high values of `frac_dev` can result in large total fluxes due to the large outer extent of the DeVaucouleus profile. Using `GAp` fluxes can be more useful, for example, when trying to estimate the photometric transfer function with a source injection scheme such as `Balrog` (S. Everett et al. 2022; D. Anbajagane et al. 2025).

Additional multiepoch processing was performed to derive a morphological object classifier based on the difference of Gaussian-weighted fluxes. Fluxes were derived using a Gaussian weight with a size matched to the PSF, and a second Gaussian with size dilated by 5%. We define the ratio of these measurements, $C_{\rm raw} = -2.5\log_{10}(F_{\rm dil}/F)$. For pointlike objects, $C_{\rm raw}$ will be equal to a particular value that depends on the PSF. This value is calibrated by performing the same measurement on the PSF model, $C_{\rm psf} = -2.5\log_{10}(F_{\rm dil,psf}/F_{\rm psf})$. We then define the concentration parameter, `CONC` $= C_{\rm psf} - C_{\rm raw}$. Pointlike objects occupy a narrow locus at `CONC` = 0, while galaxies generally have `CONC` > 0. While the `CONC` parameter was not found to perform significantly better for star–galaxy classification than a prescription based on the `BDF` fits (Section 4.2), it is very robust, and measurements of `CONC` exist for nearly all objects in the Y6 Gold catalog (in contrast, the `BDF` fits fail for ~0.2% of objects).

4. Y6 Gold Object Catalog

The DES Y6 Gold catalog is a merger of columns drawn from DES DR2, the multiepoch photometric measurements described in the previous section, and new quantities described in this section. These include corrections to the measured multiepoch photometry, star–galaxy classification, object quality flags that summarize other flags from measurement pipelines and features of the data, and a photometric redshift estimator.

4.1. Photometric Corrections

Y6 Gold includes columns for PSF and `BDF` model photometry that have been normalized to the `MAG_APER_8` system used for global photometric calibration, and dereddened with a fiducial interstellar extinction correction. These are labeled as `_CORRECTED` in the catalogs and are the most uniform across the survey footprint.

4.1.1. Aperture Corrections

The DES DR2 photometric zero-points were established by FGCM using the PSF flux measurements of stars in the single-epoch catalogs measured by `SExtractor` assuming the `PSFEx` model. These measurements are placed on the `APER_8` (5.″84 diameter aperture) system through the normalization of the `PSFEx` model. An aperture correction is necessary to place the multiepoch `fitvd` PSF and `BDF` model measurements of stars on this same photometric system. This aperture correction is estimated at the location of each catalog object using the `ngmix` Gaussian mixture model fit to the PSF (Section 3.4) and calculating the fraction of the PSF model flux contained within a 5.″84 diameter circular aperture (`APER_8`) relative to the total PSF model flux. This correction is typically ~2%, in the sense that the corrected flux in the `APER_8` system for stars is ~2% fainter than the uncorrected total PSF flux. This procedure (i.e., assuming a pointlike object) is used to calculate an aperture flux correction for all objects in the Y6 Gold catalog. The correction is reasonably accurate for very small galaxies (i.e., galaxies with angular sizes of <1″ before convolution with the PSF). However, larger galaxies have a larger fraction of their light extending beyond the `APER_8` aperture, and thus, the aperture corrections estimated assuming a pointlike source did not reduce the flux enough to make the `fitvd` model measurements match the `APER_8` measurements. Note that this aperture correction is not intended to address long-standing issues concerning how to deal with extended galaxy profiles in the calculation of total galaxy magnitudes, but rather simply ensures that the `fitvd` PSF and `BDF` magnitudes of stellar objects are on the FGCM system, and that the flux measurements converge in the small-size limit of unresolved galaxies.

4.1.2. Interstellar Extinction

The Y6 Gold table includes a column containing the $E(B-V)$ values from the reddening map of D. J. Schlegel et al. (1998; SFD98) extracted at the location of each catalog object. The $E(B-V)$ values were obtained using a linear interpolation of the zenithal equal area projected map distributed by SFD98 and are the same as provided in DES DR2. The FGCM magnitudes can be corrected by an amount $A_b = E(B-V) \times R_b$, where R_b is computed per band as described in DES Collaboration (2018) using the DES standard bandpasses. Following DES Collaboration (2018), we incorporate a renormalization of the original SFD98 reddening map ($N = 0.78$; E. F. Schlafly & D. P. Finkbeiner 2011) to our fiducial reddening coefficients so that these coefficients can be used directly with $E(B-V)$ values from the SFD98

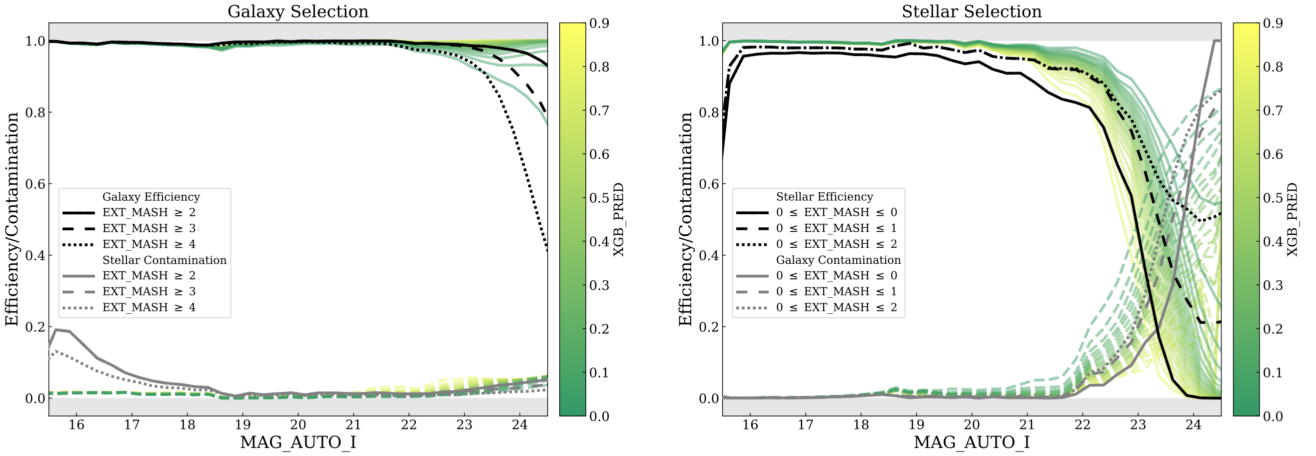

Figure 3. Performance of morphological star–galaxy classification in DES Y6 Gold, showing the galaxy selection on the left and the stellar selection on the right. The conventional cut-based classifier is shown in solid, dashed, and dotted lines for three different object selections. Black lines correspond to selection efficiency (true-positive rate), while gray lines show contamination (false-discovery rate). The green/yellow colored lines show the performance of the `XGBoost` classifier for different selections on the continuously valued XGB_PRED classifier output.

Table 3
Morphological Object Classes

Value	Description
4	Ultrapure galaxy sample
3	High-confidence galaxies
2	Mostly galaxies
1	Likely stars
0	High-confidence stars
−9	Data not available

Note. Discrete object classes assigned in the `EXT_MASH`, `EXT_FITVD`, `EXT_XGB` variables. The `EXT_COADD` and `EXT_WAVG` variables do not include class 4.

(see Section 6.4 for details on this renormalization). The values for R_b are thus the same as for DES DR1 and DR2, and are replicated here for completeness: $R_g = 3.186$, $R_r = 2.140$, $R_i = 1.569$, $R_z = 1.196$, and $R_Y = 1.048$.

4.2. Object Classification

Following previous DES analyses (e.g., DES Collaboration 2021; I. Sevilla-Noarbe et al. 2021), we define high-quality samples of pointlike objects (e.g., stars, quasars) and extended objects (e.g., galaxies) based on morphological measurements. We assign each object in the Y6 Gold catalog to a morphological class based on the multiepoch measurements, the weighted average of the single-epoch measurements, and measurements on the coadded images with larger values corresponding to higher-confidence extended objects (`EXT_MASH`; Table 3). Furthermore, we train a gradient-boosted decision tree algorithm (`XGBoost`; T. Chen & C. Guestrin 2016) on the multiepoch and single-epoch weighted average measurements to automate the classification processes (`EXT_XGB` and `XGB_PRED`). Here, we summarize the performance of these morphological classifiers, while more details can be found in Appendix A.

We assess the efficiency (true-positive rate) and contamination (false-discovery rate) of each of our output classes in the bright ($i < 18.5$ mag) and faint ($i > 18.5$ mag) domains using a high-Galactic-latitude region of the footprint. In the bright domain, we use infrared data from the Vista Hemisphere Survey (VHS DR5; R. G. McMahon et al. 2013) to classify stars and galaxies as demonstrated in I. K. Baldry et al. (2010) and I. Sevilla-Noarbe et al. (2018). We perform a $0''.5$ astrometric match between the Y6 Gold and VHS catalogs at $0° < \alpha_{2000} < 45°$ and $\delta_{2000} \sim 0°$ ($-68° < b < -48°$), and define a stellar versus nonstellar classification based on DES $(g - i)$ optical color versus VHS $(J - K_s)$ infrared color. In the faint domain, we use data from HSC-SSP PDR3 deep/ultradeep SDSX field (H. Aihara et al. 2022), which is located at α_{2000}, $\delta_{2000} \sim 35^\circ\!.8, -4^\circ\!.6$ ($b \sim -58^\circ\!.5$) and has superior depth and image resolution ($0''.75$ median). We perform a $0''.5$ astrometric match between the Y6 Gold and HSC-SSP catalogs, and define stellar versus nonstellar classifications based on the HSC-SSP concentration parameter defined as the difference between the `i_psfflux_mag` and the `i_cmodel_mag` following the prescription described in DES Collaboration (2018) and A. Drlica-Wagner et al. (2021).

Figure 3 shows the efficiency (true-positive rate) and contamination (false-discovery rate) of the DES Y6 Gold-`EXT_MASH` and `XGBoost` classifiers compared to the VHS-based color classification at the bright end ($i < 18.5$ mag) and HSC-SSP PDR3 morphological classification at the faint end ($i > 18.5$ mag). Black and gray lines show the efficiency and contamination, respectively, for the conventional cut-based `EXT_MASH` classifier, with different line styles corresponding to different object classes, as detailed in the legend of Figure 3. In addition, the green/yellow lines show the efficiency/contamination of a broad range of object classes that can be defined based on the continuous `XGBoost` predictor output, `XGB_PRED`. Similarly to DES Y3 Gold, we see an increase in the stellar contamination in the bright galaxy sample at `MAG_AUTO_I` <19 mag. This increase in contamination is partially driven by the increasing fraction of stars in the object sample at bright magnitudes, in addition to contamination from double stars that are morphologically extended but classified as stars based on their infrared colors. Interestingly, we find that the morphological `XGBoost` classifier is much more robust to this contamination at the bright end, suggesting that these contaminants occupy a distinct region of the morphological parameter space, which can be identified through more complex machine learning techniques. The Y6 Gold ultrapure galaxy class (`EXT_MASH` = 4) achieves 90% completeness for

Table 4
Summary of Bitmask Values and Warning Descriptions for the `FLAGS_GOLD` Column

Bit	Number of Objects Affected	Description
1	1,388,296 (0.2%)	`fitvdFLAGS` != 0, Indicates problems in `fitvd` processing
2	833,130 (0.1%)	Any `SExtractorFLAGS_{GRIZ}`$>$ 3, Standard `SExtractor` quality selection
4	2,830,733 (0.4%)	Any of `SExtractor IMAFLAGS_ISO_{GRIZ}` != 0, Saturated objects
8	11,444,931 (1.7%)	Superspreader objects; `BDF_T` * `BDF_T_ERR` $>$ 30 and `BDF_T` / `BDF_T_ERR` $<$ 3
16	41,483,901 (6%)	Possible noise objects; any of *riz* magnitudes approximately below the S/N ≈1 threshold (as determined by exposure time calculations)
32	8,627,937 (1.2%)	Extreme color outliers; $r - i$ or $i - z$ colors outside the $[-5, 5]$ range
64	240,448 (0.03%)	Phantom objects; objects with `NEPOCHS`=0 for all bands and `MU_EFF_MODEL` $>$ 26 for *riz* bands, but with `MAG_AUTO_I` $<$ 22

galaxies at a magnitude 0.5 mag fainter than Y3 Gold does, with no increase in contamination. Nonetheless, cosmological analyses that require a very pure sample of galaxies may consider using additional color cuts to remove bright contaminants from the galaxy sample (see, for example, N. Weaverdyck et al. 2026).

Appendix A discusses the relative performance of these classifiers, with Table A3 providing a summary.

4.3. Object Quality Flags

The `FLAGS_GOLD` column is a bitmask used to identify objects that present unusual features in the measurement process or that are deemed unphysical. Flagged objects can be excluded as appropriate for a given analysis using bitwise operations. The `FLAGS_GOLD` bits and the number of affected objects can be found in Table 4. Several object quality flag categories are defined to indicate objects with potentially suspect measurements. The approach taken in Y6 Gold is similar to that applied in Y3 Gold, and dominantly focuses on the `fitvd` (formerly MOF/SOF) and `SExtractor` processing flags. Several additional bits have been added to flag other types of spurious objects and objects with compromised photometry, which we describe below. We expect that most science applications will select objects with `FLAGS_GOLD` = 0, which includes 635,487,439 objects in the full catalog.

A new class of flagged objects with suspect measurements in Y6 Gold, so-called “superspreader” objects, are identified as having extremely large sizes and large size measurement uncertainty when measured by `fitvd`. These objects were initially identified in Y3 synthetic source injection analyses (see Figure 21 of S. Everett et al. 2022) and subsequently in the Y6 redMaGiC sample as outliers possessing much-too-large photometric uncertainty relative to their brightness (see E. Rozo et al. 2016, for a description of the redMaGiC sample). We attribute these fitting failures to catastrophic overestimation of the object size that occurs more frequently in crowded fields and regions with structured diffuse light (Appendix C.1).

We flag another class of “noise objects” that are sufficiently faint to have a predicted S/N smaller than unity. To identify these objects, we defined flux thresholds using the DECam exposure time calculator assuming a lunar phase of 10 days after new Moon and the approximate integrated exposure time of the DES coadds (900 s). Objects in the DES Wide-Field Survey with measured magnitudes fainter than the AB magnitude thresholds of $\{r, i, z\} = \{26.5, 26.2, 25.6\}$ mag are flagged as likely noise artifacts. Note that this selection may remove r-band outliers that may be of interest for certain analyses. Extreme color outliers are defined to catch lingering reflections and residual noise artifacts that would hinder photo-z estimates. This flag is found to be very correlated with the noise objects. For similar reasons, we use the *riz* detection bands and define color outliers as any of the colors $r - i$ or $i - z$ to fall outside the $[-5, 5]$ range, using the AUTO magnitudes.

Phantom objects are objects that have a bright magnitude in coadds, but have not been detected in individual single epochs. These are coming mostly from diffraction spikes and excess light around bright stars.

4.4. Photometric Redshifts

The Y6 Gold catalog provides default photometric redshift estimates for every object based on their `fitvd`-corrected (by extinction and aperture) magnitudes and colors. These estimates are based on the directional neighborhood fitting (DNF; J. De Vicente et al. 2016) code, which was successfully applied to and validated on the DES Y3 data (I. Sevilla-Noarbe et al. 2021; L. Toribio San Cipriano et al. 2024). It uses a nearest-neighbor approach with a directional metric that accounts simultaneously for magnitudes and colors to obtain the photometric redshift for each object (`DNF_Z`) using around 80 neighbors (`DNF_NNEIGHBORS`), using a spectroscopic reference dataset. The photo-z error (`DNF_ZSIGMA`) is estimated as the quadratic mean of the uncertainty due to photometric errors (`DNF_ZERR_PARAM`) and the uncertainty obtained from the residuals of the fit (`DNF_ZERR_FIT`). On the other hand, only the single nearest neighbor is used to provide a point value (`DNF_ZN`) to construct an $N(z)$ estimate. Other approaches relying on calibration with deep fields (e.g., J. Myles et al. 2021; G. Giannini et al. 2024) may be used additionally for these distributions, and will be released in the corresponding analyses.

Figure 4 shows some standard photo-z metrics for a Y3 and Y6 Gold selection matched to a spectroscopic data sample. This dataset has been compiled with the framework described in J. Gschwend et al. (2018) and includes 545,796 spectroscopic redshifts deemed of optimal quality (`FLAG_DES` = 4, according to the classification in J. Gschwend et al. 2018). Note that the spectroscopic sample is brighter than Y6 Gold, and further studies are required to understand its performance in detail (e.g., W. G. Hartley et al. 2020). The lens sample for the combined weak lensing and galaxy clustering analyses, as well as the galaxy sample used for measurements of baryon acoustic oscillations, are drawn from intermediate depth samples of Y6 Gold ($i \lesssim 22.5$ mag) for which these metrics would approximately apply. Most of the relevant galaxies (i.e.,

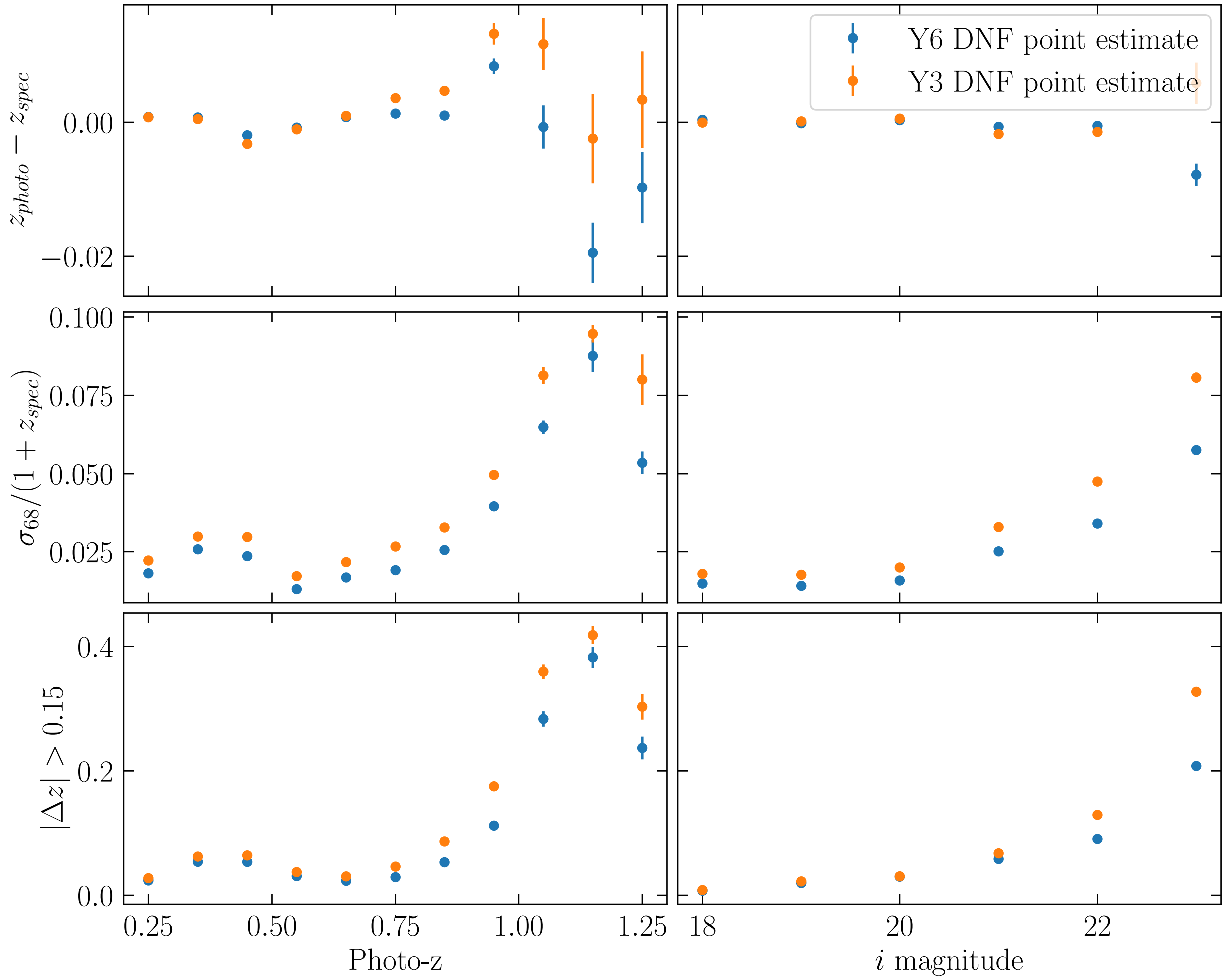

Figure 4. Photometric redshift metrics for the DNF point estimate included in Y3 and Y6 Gold. The upper row corresponds to the bias measured with the median per photo-z or magnitude bin. The middle row is the scatter measured with the 68th percentile range around the mean. The bottom row is the outlier rate, measured as objects with a bias larger than 0.15 (which increases as expected with larger scatter). These metrics are similar in format to what is presented in J. L. van den Busch et al. (2020).

galaxies in the magnitude range of interest) from the spectroscopic reference dataset come from public releases such as SDSS DR16 (62%; R. Ahumada et al. 2020) or 2dF (9%; M. Colless et al. 2003), with deeper and narrower surveys covering the fainter magnitudes such as DEEP2 (2%; J. A. Newman et al. 2013) and VVDS (1%; O. Le Fèvre et al. 2013). VIPERS also constitutes a major source of moderate to faint galaxies with a very broad color coverage (5%; M. Scodeggio et al. 2018). DES specific proprietary programs were done using AAOmega on the AAT to complement these spectra (3%; C. Lidman et al. 2020). Finally, an assortment of other shallow and deep datasets were included as well, for increased color and redshift coverage.

5. Ancillary Maps

In addition to the object catalog, the Y6 Gold dataset includes several maps of the survey geometry, survey properties, and astrophysical foregrounds that complement the interpretation of the catalogs. A technical advance introduced in Y6 Gold is the use of the `healsparse`[74] software to store the map and mask data. `healsparse` is a sparse implementation of `HEALPix` in Python that optimizes memory usage by using a coarser resolution in those areas of the sky that are not covered. In the case of Y6 Gold, this allows for practical usage of maps with `HEALPix` resolution of `nside` = 16,384 corresponding to pixels of area 0.046 arcmin^2. The enhanced resolution is sufficient for detailed representation of the gaps between sensors on the DECam focal plane mosaic as well as masked regions around individual bright stars (Figure 5).

The maps described in this section include the survey footprint (Section 5.1), a mask of astrophysical foregrounds (Section 5.2), survey property maps (Section 5.3), and a mask of diffuse foregrounds (i.e., Galactic cirrus and nebulosity; Appendix C.1).

5.1. Footprint

The Y6 Gold footprint is a description of the angular mask that contains the regions of the sky that are deemed useful for cosmological analyses with the Y6 Gold catalog. The source of “truth” for which parts of the sky have been observed are `mangle` (M. E. C. Swanson et al. 2008) files that describe in detail the nature of the geometry of the CCDs on overlapping exposures for each band. In turn, these complex, high-resolution maps are represented into a standardized `HEALPix` map of `nside` = 16,384 resolution, which represents the

---

[74] https://healsparse.readthedocs.io

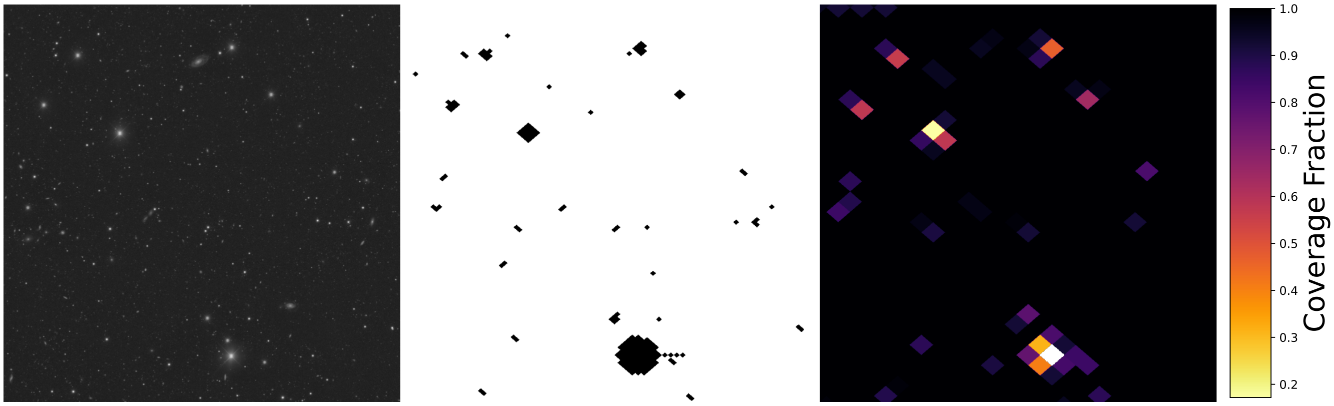

Figure 5. A side-by-side comparison of the different footprint resolutions using tile DES0219−0541 in the g band as an example. The coadd image is shown as a reference on the left. In the middle panel, the binary mask at the highest resolution available in Y6 Gold is shown (`nside` = 16,384). Finally, the coarser resolution (`nside` = 4096) mask with approximate coverage fraction is shown on the right. This coverage fraction represents how many high-resolution subpixels contain valid information for this band.

underlying survey geometry at suitable accuracy for our needs. The Y6 Gold footprint then is represented via a binary `healsparse` file of `nside` = 16,384 resolution, constructed by applying certain conditions on survey property maps. These include:

1. At least two exposures in each of g, r, i, and z in the `nexp_sum` survey property map.
2. $f_{griz} > 0.5$, where f_{griz} is the fraction of each pixel that has simultaneous coverage in the four bands when considering `nside` = 4096 pixels, which is used for compatibility purposes as some Y3 analyses used this coarser version. This quantity is obtained from the `FRACDET_GRIZ` map.

A footprint map with only the two-exposure condition is also made available. For the case of the coarse `nside` = 4096 footprint version, a complementary map with the same resolution is available, denoting the fraction of each pixel that has simultaneous coverage in the four bands ($0 \leqslant f_{griz} \leqslant 1$).

Each object in Y6 Gold has an associated `FLAGS_FOOTPRINT` value that is equal to the footprint map value at the position of the object (using the full-resolution `ALPHAWIN_J2000`, `DELTAWIN_J2000` coordinates) provided that the object also has the `SExtractor` quantities `NITER_MODEL_{G,R,I,Z}` > 0 for every band. This ensures that the object indeed has the observations in all four bands, in case it happens to be in one of the residual regions of a valid footprint pixel, lacking some of the observations in the key bands. The total Y6 Gold footprint area using the high-resolution map with the conditions described above is 4923.21 $\deg^2$. The Y6 Gold area computed in this way is slightly larger than the DES DR2 area (4913 $\deg^2$), which was estimated requiring at least one exposure in each of the five $grizY$ bands.

The Y6 Gold footprint area is slightly smaller than the Y3 Gold footprint area, 4945.87 $\deg^2$. This is a result of the increase of both the survey depth and the threshold for minimum number of exposures (changed from one to two) between the two releases.

For a threshold of two exposures in each of g, r, i, and z, the equivalent footprint area for Y3 Gold is 4495.26 $\deg^2$, demonstrating the increase in coverage from Y3 to Y6 Gold.

5.2. Foreground Mask

Y6 Gold includes a mask to identify regions of the footprint that are likely to be impacted by the presence of bright astrophysical foreground objects, shown in Figure 6. Similar to Y3 Gold, we define the foreground mask for bright stars, globular clusters, and nearby galaxies. For bright stars, we mask regions from a magnitude-dependent radius that was derived from the density of DES Y6 objects where the i-band magnitude measured by the bulge–disk fit is much brighter than that `SExtractor-AUTO` measurement (i.e., `BDF_MAG_I-MAG_AUTO_I`<−1).

This mask is constructed as a `HEALPix` bit map (`nside` = 4096), and catalog objects are assigned a `FLAGS_FOREGROUND` value corresponding to the sum of the bits in that position of the map, according to their sky coordinates (α_{2000}, δ_{2000}). In cases where the mask radius is smaller than a single `HEALPix` pixel, the pixel containing the object is used as the mask. The specific bits in the foreground mask are defined in Table 5. A `healsparse` high-resolution map (`nside` = 16,384) is also made available upon release, though `FLAGS_FOREGROUND` in the table does not follow this convention.

1. *Bit 1, Gaia bright stars:* bright stars from Gaia DR2 ($G < 7$) were masked based on the G-band magnitude.
2. *Bit 2, Yale bright star catalog:* stars from the Yale Bright Star Catalog (D. Hoffleit & C. Jaschek 1991) were masked based on the V-band magnitude.
3. *Bit 4, 2MASS bright stars:* bright stars ($4 < J < 8$) magnitude from the Two Micron All Sky Survey (2MASS) catalog (M. F. Skrutskie et al. 2006) were masked based on the J-band magnitude.
4. *Bit 8, Gaia moderately bright stars:* moderately bright stars ($7 < G < 11.5$) from Gaia DR2 were masked based on the G-band magnitude.
5. *Bit 16, 2MASS moderately bright stars:* moderately bright ($8 < J < 12$) stars from the 2MASS catalog (M. F. Skrutskie et al. 2006).
6. *Bit 32, Bright galaxies:* area around large, nearby galaxies found in the HyperLEDA[75] catalog (D. Makarov et al. 2014).

---

[75] http://leda.univ-lyon1.fr/

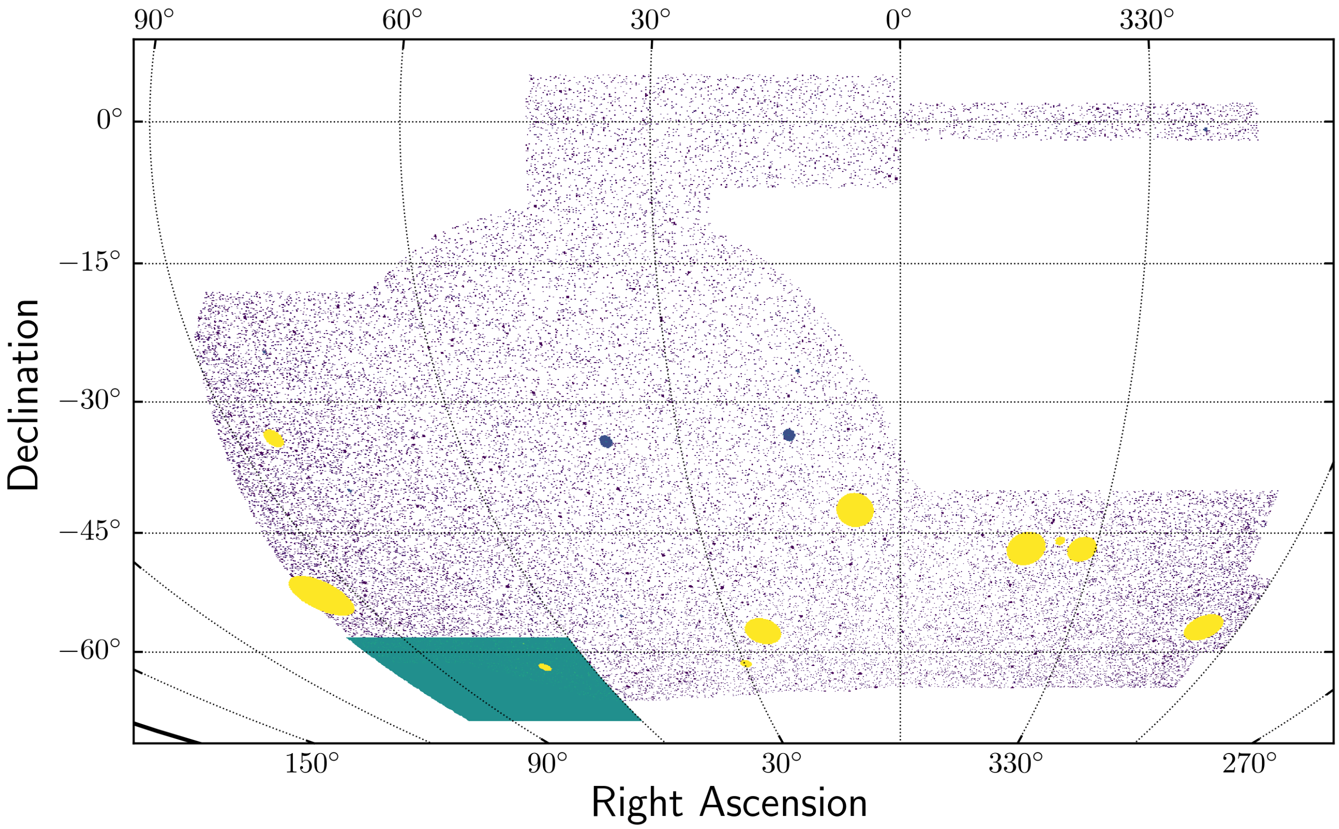

Figure 6. The foreground mask for Y6 Gold. The region close to the LMC appears in turquoise, very bright stars appear in yellow Table 7), while the Milky Way satellite galaxies Fornax and Sculptor can be seen in dark blue at decl. ~ -35 deg. Small regions around a variety of bright stars and nearby galaxies are masked in purple. See Section 5.2 for details.

Table 5
Y6 Gold Foreground Region Mask

Flag Bit	Area (deg^2)	Description
1	36.4	Gaia bright stars ($G < 7$)
2	19.7	Yale bright stars
4	78.3	2MASS bright stars ($4 < J < 8$)
8	158.1	Gaia moderately bright stars ($7 < G < 11.5$)
16	254.6	2MASS moderately bright stars ($8 < J < 12$)
32	18.9	HyperLEDA bright galaxies
64	0.4	Milky Way satellites (Table 6)
128	102.8	Large Magellanic Cloud periphery
256	76.2	Very bright stars (Table 7)

Note. The masked area from the Y6 Gold catalog is calculated using the coverage fraction of the pixels that are removed from the footprint by each mask. The rationale for each mask can be found in Section 5.2.

7. *Bit 64, Milky Way satellites:* Milky Way globular clusters and classical dwarf spheroidal galaxies in the footprint were masked (Table 6).
8. *Bit 128, Large Magellanic Cloud (LMC) periphery:* the periphery of the LMC ($60 < \alpha_{2000} < 100$ deg and $-70 < \delta_{2000} < -58$ deg) was masked due to the significant increase in the number density of stars.
9. *Bit 256, Very bright stars:* very bright stars that produce significant scattered light artifacts were explicitly masked to remove areas with high densities of objects with anomalous colors. These stars are listed in Table 7.

Table 6
Milky Way Globular Clusters and Satellite Galaxy Exclusion List

Name	α_{2000}, δ_{2000} (deg, deg)	Radius (deg)
AM 1	(58.7612, −49.6144)	0.015
Eridanus	(66.1854, −21.1869)	0.015
Fornax	(39.9971, −34.4492)	0.7
NGC 0288	(13.1979, −26.59)	0.2
NGC 1261	(48.0637, −55.2169)	0.15
NGC 1851	(78.5262, −40.0472)	0.2
NGC 1904	(81.0442, −24.5242)	0.17
NGC 7089	(323.375, −0.8167)	0.22
Reticulum	(69.0375, −58.85833)	0.08
Sculptor	(15.03875, −33.7092)	0.7
Whiting 1	(30.7375, −3.25277)	0.015

Note. AM1, Eridanus, and Whiting 1 have angular sizes that are smaller than a single `nside` =4096 `HEALPix` pixel. Thus, their mask radius is set to the approximate angular size of a pixel.

The magnitude-dependent radii for the Gaia, Yale, and 2MASS masks were defined based on a cumulative plot of the ratio of objects with inconsistent `BDF` and `AUTO` magnitudes as a function of distance to the bright sources. These “bad” objects are associated with image artifacts around the bright source locations. The mask radii were determined by inspection such that spurious objects are subdominant beyond the masked regions. Further quality cuts with `FLAGS_GOLD` eliminate additional objects outside these masks. The LMC

Table 7
Very Bright Stars Included in the Foreground Mask

Name	α_{2000}, δ_{2000} (deg, deg)	Radius (deg)
α Phe	(6.5708, −42.3061)	2.0
α Eri	(24.4288, −57.2367)	1.7
α Hyi	(29.6925, −61.5697)	0.5
α Col	(84.9121, −34.0741)	1.0
α Car	(95.9879, −52.6958)	2.5
α Pav	(306.41214, −56.7350)	1.7
α Gru	(332.0583, −46.9611)	1.5
β Gru	(340.6671,−46.8847)	2.0
Pi1 Gru	(335.6829, −45.9478)	0.5
R Dor	(69.1900, −62.0775)	0.5

Note. The third column indicates the masking radius applied for each case.

and very bright star masks were defined on an ad hoc basis by visual inspection.

5.3. Survey Properties

Survey property maps represent spatially varying distributions of observation characteristics and astrophysical line-of-sight effects that systematically impact the detection and measurement of sources across the footprint, and consequently affect statistical analysis of the large-scale distribution of galaxies (e.g., M. Rodríguez-Monroy et al. 2022). The Y6 Gold survey property maps are distributed in both `HEALPix` and in `healsparse` formats. In both cases, the map content is derived from `mangle` polygon masks that encode the full-resolution coadd image geometry. The full list of survey property maps can be found in Appendix C.

6. Caveats and Known Issues

6.1. Background Offset

Y6 Gold photometry is impacted at a low level by both global and local background oversubtraction that is likely attributed to the extended PSF of bright stars and galaxies, coupled with the spatial scale of sky background estimation. The effect can be recognized through ratios of `SExtractor` aperture fluxes measured for two different aperture radii averaged over a large number of test stars. In the case of ideal background modeling and a fixed PSF, this ratio should be independent of both the flux of the stars used for the test and their spatial location within the footprint. For Y6 Gold, we find that the ratio of aperture fluxes exhibits a flux dependence, with the large-aperture photometry of fainter stars being more impacted by background oversubtraction. The amplitude of the background offset is correlated with the density of bright stars across the survey footprint. The largest oversubtraction occurs at an angular separation of $1'$–$2'$ around bright stars and galaxies, corresponding to the $1\overset{'}{.}1 \times 1\overset{'}{.}1$ gridding scale used for background estimation. Analysis suggests that the extended wings of the PSF are being treated as a background, resulting in oversubtraction relative to the natural sky level.

6.2. Spurious Sources and Catastrophic Measurement Errors

Removing superspreader objects (`FLAGS_GOLD` = 8) was found to be potentially problematic for the analyses of galaxies in the central regions of galaxy clusters. Some modifications were introduced to mitigate this problem in the final Y6 Gold catalog. However, specific care is advised for the study of galaxies in dense environments, including comparative tests with and without the superspreader cut.

6.3. FITVD Failures

Three tiles (DES0456-5705, DES0456-5705, and DES0424-3249) experienced partial corruption during the main `fitvd` run. This led to spatially correlated failures of the `fitvd` measurements. Some cosmology papers (e.g., DES Collaboration 2024a) used an earlier version of Y6 Gold that masked out these three tiles, corresponding to a loss of 1.5 $\deg^2$ (0.03% of the footprint area). Complete measurements for those three tiles were restored for the final version of Y6 Gold released here.

6.4. Extinction

As described in Section 4.1.2, the R_b coefficients provided by the DES data releases apply a renormalization of $N = 0.78$ to the measured $E(B-V)$ values from SFD98. This renormalization was originally suggested by E. F. Schlafly et al. (2010) and was later used to calculate the R_b values in Table 6 of E. F. Schlafly & D. P. Finkbeiner (2011). However, E. F. Schlafly & D. P. Finkbeiner (2011) suggested that a renormalization of $N = 0.86$ may be more appropriate in low-reddening regions that have $E(B-V) < 0.2$, which is the case for most of the DES footprint. Users may easily rescale the R_b extinction values provided by Y6 Gold with their preferred renormalization of the SFD98 maps.

7. Using Y6 Gold

The Y6 Gold data products and user documentation are publicly available at https://des.ncsa.illinois.edu/releases alongside previous major DES releases. A selection of the most important columns of the catalog is provided in Appendix B. Y6 Gold includes the value-added object catalog together with maps detailed in Section 5 in `HEALPix` and `healsparse` formats.

General usage recommendations are listed below:

1. Use `FLAGS_FOOTPRINT` = 1 to select objects located within the standard Y6 Gold footprint, as described in Section 5.1.
2. Regions with astrophysical foregrounds identified in Section 5.2 can present various problems in terms of photometry, spurious detections, obscuration, etc. The `FLAGS_FOREGROUND` = 0 selection is generally recommended for extragalactic studies.
3. As explained in Section 4.3, `FLAGS_GOLD` facilitates the selection of good-quality objects by summarizing various flags and signatures of poor reconstructions in a single bitmask. A `FLAGS_GOLD` = 0 selection will suffice for most applications.
4. All photometry measurements include atmospheric and instrumental calibration derived from FGCM (i.e., top-of-the-atmosphere photometry; Section 3.2). By default, reported fluxes/magnitudes are NOT corrected for interstellar dust extinction. Final top-of-the-Galaxy photometry can be obtained by applying an aperture correction and fiducial de-reddening (Section 4.1); only

the measurements with the `_CORRECTED` suffix take into account these two adjustments.

5. The `EXT_MASH` star/galaxy separator is expected to be appropriate for most scientific applications. This classifier is based on morphological quantities, as described in Section 4.2 and Appendix A.1. The method employs `EXT_FITVD` as the main classifier for an object, but reverts to `EXT_WAVG` or `EXT_COADD` measurements as necessary. For cosmology analyses, the selection `EXT_MASH` = 4 is a recommended starting point, since it shows low stellar contamination up to the magnitude limit, with a decrease in galaxy selection efficiency only beyond $i > 22.5$ mag. The outputs of the `XGBoost` classifier (`EXT_XGB` and `XGB_PRED`) have been found to outperform `EXT_MASH`, but have received much less validation in the context of cosmological analyses.

The Y6 Gold data used for most Y6 cosmology analyses corresponds to DES internal version 2.2.

8. Summary and Outlook

The Y6 Gold data products presented here, together with weak lensing shear (M. Yamamoto et al. 2025) and Deep Field (R. Gruendl et al. 2026, in preparation) catalogs, form the foundation of legacy static-sky cosmology from the full observational dataset of DES. Components of the final Y6 Gold release, summarized in Table 2, include:

1. A catalog of 669 million high-quality objects covering $\sim$5000 deg^2 of the southern Galactic cap to a depth of $i_{AB} \sim 23.4$ at S/N $\sim$ 10 for extended objects with measurements in the *grizY* bands derived from the DES Wide-Field Survey data released in DES DR2 (DES Collaboration 2021).
2. Flux measurements for PSF, `BDF`, and `GAp` models derived from simultaneous fits to multiepoch, multiband photometry to enable more robust determination of colors and morphology.
3. Per-object aperture corrections and interstellar extinction estimates to take full advantage of top-of-the-atmosphere photometric uniformity of <2 mmag.
4. Improved morphological object classification schemes based on both conventional and machine learning approaches.
5. Photometric redshifts derived with the DNF estimator (J. De Vicente et al. 2016).
6. An expanded set of per-object flags to select reliable object samples.
7. Foreground mask to select recommended regions for extragalactic studies.
8. High-resolution footprint and survey property maps representing the observational coverage and properties of the DES dataset.

These curated and validated data products will enable some of the tightest constraints on the standard cosmological model to date, and are well suited for detailed statistical analyses of extragalactic populations and the Milky Way stellar halo. Data products and documentation are publicly available at https://des.ncsa.illinois.edu/releases.

A new generation of wide-area imaging surveys will soon advance our understanding of new physics implied by cosmological observations and theory. Ground-based surveys including the Vera C. Rubin Observatory's LSST will catalog $>10^{10}$ galaxies and $>10^5$ SNe Ia (Ž. Ivezić et al. 2019). The Euclid (Euclid Collaboration 2024) and Nancy Grace Roman (D. Spergel et al. 2015) observatories will use high-resolution space-based imaging to cover complementary spatial regions, depth ranges, and wavelengths. Meeting the statistical grasp of these new projects to make accurate cosmological inferences will require even more stringent control of systematic effects related to the detectors, atmosphere, and survey observations. DES has been an important development and testing ground for pixel-level processing, calibration, and measurement algorithms, several of which are now being incorporated into the LSST Science Pipelines (J. Bosch et al. 2018, 2019) including methods for representing survey geometry and metadata (`healsparse`), PSF modeling (`PIFF`), photometric calibration (FGCM), astrometric calibration with simultaneous solution across bands and coadd input images, survey-scale synthetic source injection (`Balrog`), cell-based coaddition, weak lensing shear measurement (`metadetection`, `BFD`), and usage of deep field processing for accurate shape and color references for the wide survey. Compelling science questions, new observational capabilities, and continuously improving methods for data management and analysis promise an exciting future for wide-area imaging surveys for years to come.

Acknowledgments

We thank Lynne Jones and Jean-Charles Cuillandre for help with the LSST and Euclid footprints.

Contribution statement: K.B. led the Y6 Gold development and contributed to manuscript writing; I.S.-N. contributed to catalog and mask creation and manuscript writing; A.D.-W. developed the XGB star/galaxy classifier and contributed to manuscript writing; B.Y. and R.A.G. led many technical aspects of the DES Data Management production and contributed to manuscript writing; E.Sh. designed the `fitvd` and `ngmix` algorithms and contributed to the manuscript. Authors E.S.R., J.d.V., M.Ad., D.A., M.R.B., G.M.B., A.C.R., J.G., M.Go., W.G.H., M.J., T.J., R.K., T.A.M., J.O'D., A.Pi., M.R.-M., D.S.C., M.T., L.T.S.C., D.L.T., N.W., and M.Y. contributed to various aspects of assembling and validating Y6 Gold including the creation of specific data products, scientific validation, manuscript writing, manuscript review, data product documentation, and data release, as well as coordinating the processes mentioned above. The remaining authors have made contributions to this paper that include, but are not limited to, the construction of DECam and other aspects of collecting the data; data processing and calibration; developing broadly used methods, codes, and simulations; running the pipelines and validation tests; and promoting the science analysis. W.G.H. and R.K. served as internal reviewers for the manuscript.

Funding for the DES Projects has been provided by the U.S. Department of Energy, the U.S. National Science Foundation, the Ministry of Science and Education of Spain, the Science and Technology Facilities Council of the United Kingdom, the Higher Education Funding Council for England, the National Center for Supercomputing Applications at the University of Illinois at Urbana-Champaign, the Kavli Institute of Cosmological Physics at the University of Chicago, the Center for Cosmology and Astro-Particle Physics at the Ohio State

University, the Mitchell Institute for Fundamental Physics and Astronomy at Texas A&M University, Financiadora de Estudos e Projetos, Fundação Carlos Chagas Filho de Amparo à Pesquisa do Estado do Rio de Janeiro, Conselho Nacional de Desenvolvimento Científico e Tecnológico and the Ministério da Ciência, Tecnologia e Inovação, the Deutsche Forschungsgemeinschaft, and the Collaborating Institutions in the DES.

The Collaborating Institutions are Argonne National Laboratory, the University of California at Santa Cruz, the University of Cambridge, Centro de Investigaciones Energéticas, Medioambientales y Tecnológicas-Madrid, the University of Chicago, University College London, the DES-Brazil Consortium, the University of Edinburgh, the Eidgenössische Technische Hochschule (ETH) Zürich, Fermi National Accelerator Laboratory, the University of Illinois at Urbana-Champaign, the Institut de Ciències de l'Espai (IEEC/CSIC), the Institut de Física d'Altes Energies, Lawrence Berkeley National Laboratory, the Ludwig-Maximilians Universität München and the associated Excellence Cluster Universe, the University of Michigan, NSF NOIRLab, the University of Nottingham, The Ohio State University, the University of Pennsylvania, the University of Portsmouth, SLAC National Accelerator Laboratory, Stanford University, the University of Sussex, Texas A&M University, and the OzDES Membership Consortium.

Based in part on observations at NSF Cerro Tololo Inter-American Observatory at NSF NOIRLab (NOIRLab Prop. ID 2012B-0001; PI: J. Frieman), which is managed by the Association of Universities for Research in Astronomy (AURA) under a cooperative agreement with the National Science Foundation.

The DES data management system is supported by the National Science Foundation under grant Nos. AST-1138766 and AST-1536171. The DES participants from Spanish institutions are partially supported by MICINN under grants PID2021-123012, PID2021-128989 PID2022-141079, SEV-2016-0588, CEX2020-001058-M, and CEX2020-001007-S, some of which include ERDF funds from the European Union. IFAE is partially funded by the CERCA program of the Generalitat de Catalunya.

We acknowledge support from the Brazilian Instituto Nacional de Ciênciae Tecnologia (INCT) do e-Universo (CNPq grant 465376/2014-2).

This work has made use of data from the European Space Agency (ESA) mission Gaia (https://www.cosmos.esa.int/gaia), processed by the Gaia Data Processing and Analysis Consortium (DPAC, https://www.cosmos.esa.int/web/gaia/dpac/consortium). Funding for the DPAC has been provided by national institutions, in particular the institutions participating in the Gaia Multilateral Agreement.

This paper makes use of observations obtained as part of the VISTA Hemisphere Survey, ESO Program, 179.A-2010 (PI: McMahon).

The Hyper Suprime-Cam (HSC) collaboration includes the astronomical communities of Japan and Taiwan, and Princeton University. The HSC instrumentation and software were developed by the National Astronomical Observatory of Japan (NAOJ), the Kavli Institute for the Physics and Mathematics of the Universe (Kavli IPMU), the University of Tokyo, the High Energy Accelerator Research Organization (KEK), the Academia Sinica Institute for Astronomy and Astrophysics in Taiwan (ASIAA), and Princeton University. Funding was contributed by the FIRST program from the Japanese Cabinet Office, the Ministry of Education, Culture, Sports, Science and Technology (MEXT), the Japan Society for the Promotion of Science (JSPS), Japan Science and Technology Agency (JST), the Toray Science Foundation, NAOJ, Kavli IPMU, KEK, ASIAA, and Princeton University.

This paper is based on data collected at the Subaru Telescope and retrieved from the HSC data archive system, which is operated by the Subaru Telescope and Astronomy Data Center (ADC) at NAOJ. Data analysis was in part carried out with the cooperation of Center for Computational Astrophysics (CfCA), NAOJ. We are honored and grateful for the opportunity of observing the Universe from Maunakea, which has cultural, historical, and natural significance in Hawaii.

This paper makes use of software developed for Vera C. Rubin Observatory. We thank the Rubin Observatory for making their code available as free software at http://pipelines.lsst.io/.

This manuscript has been authored by Fermi Research Alliance, LLC under contract No. DE-AC02-07CH11359 with the U.S. Department of Energy, Office of Science, Office of High Energy Physics.

Facility: Blanco (DECam).

Software: `astropy` (Astropy Collaboration 2013), `decasu`,[76] `DNF` (J. De Vicente et al. 2016),[77] `easyaccess` (M. Carrasco Kind et al. 2019), `fitsio`,[78] `fpack` (W. D. Pence et al. 2010), `HEALPix` (K. M. Górski et al. 2005),[79] `healpy` (A. Zonca et al. 2019),[80] `healsparse`,[81] `mangle` (A. J. S. Hamilton & M. Tegmark 2004; M. E. C. Swanson et al. 2008), `matplotlib` (J. D. Hunter 2007), `numpy` (S. Van Der Walt et al. 2011), `PSFEx` (E. Bertin 2011), `PIFF` (M. Jarvis et al. 2021), `SCAMP` (E. Bertin 2006), `scipy` (P. Virtanen et al. 2020), `skyproj`,[82] `SExtractor` (E. Bertin & S. Arnouts 1996), `SWarp` (E. Bertin et al. 2002; E. Bertin 2010), `TOPCAT` (M. B. Taylor 2005), `XGBoost` (T. Chen & C. Guestrin 2016).

Appendix A
Object Classification

The DES Y6 Gold morphological objects classification scheme follows from similar schemes developed for DES Y3 Gold (I. Sevilla-Noarbe et al. 2021) and DES DR2 (DES Collaboration 2021). This approach defines independent object classes based on the multiepoch `fitvd` measurements, the weighted average of the `SExtractor` measurements on the individual images, and the `SExtractor` measurements on the coadded images. These independent classifications are then combined hierarchically to provide a single classification for every object in DES Y6 Gold. In addition, DES Y6 Gold includes a gradient-boosted decision tree model that incorporates morphological information in an automated classification procedure. The continuously valued output of the `XGBoost` model is divided into discrete object classes that roughly match the completeness of the conventional classifier. We discuss each of these classification approaches in more detail below.

---

[76] https://github.com/erykoff/decasu

[77] https://github.com/ltoribiosc/DNF_photoz

[78] https://github.com/esheldon/fitsio

[79] http://healpix.sourceforge.net

[80] https://github.com/healpy/healpy

[81] https://healsparse.readthedocs.io/en/latest/

[82] https://github.com/LSSTDESC/skyproj

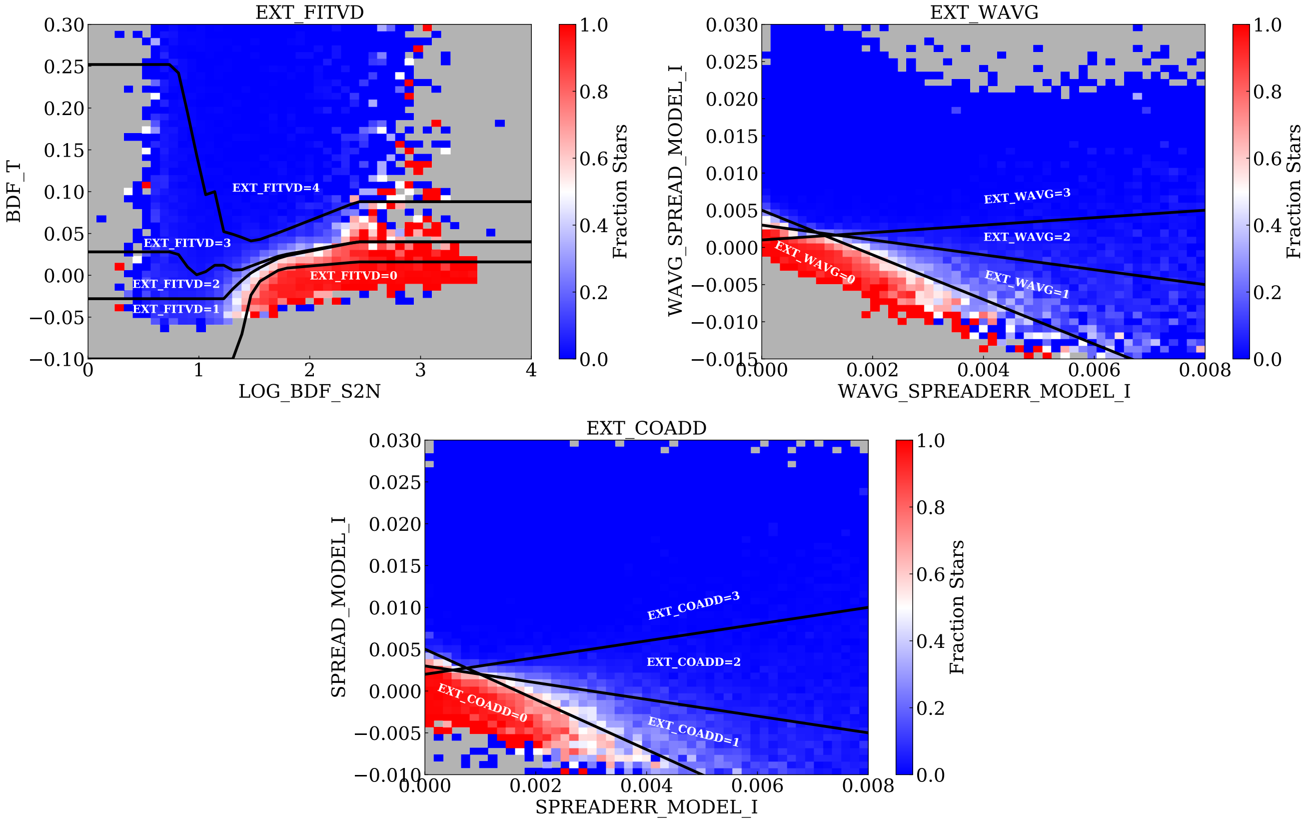

Figure A1. Conventional star/galaxy classes are defined in pairs of morphological parameters from the `fitvd` (left), `WAVG` (middle), or `COADD` (right) measurements. Each panel shows the two-parameter space where the extended classes are defined. The background color indicates the fraction of objects classified as stars using a morphological selection from HSC PDR2 and infrared data from CLAUDS in the XMM-LSS field (G. Desprez et al. 2023).

A.1. Conventional Classifiers

Independent object classifications are derived from the multiepoch `fitvd` measurements (`EXT_FITVD`), the weighted average of `SExtractor` measurements on the individual images (`EXT_WAVG`), and the `SExtractor` measurements on the coadded images (`EXT_COADD`). Each classifier assigns an integer value from 0 to 4, with 0 being high-confidence stars/QSOs, and 4 being high-confidence galaxies. When the class cannot be computed based on the specific measurement technique, a default value of −9 is assigned. These independent classifications are combined hierarchically to provide a classification for every object in DES Y6 Gold (`EXT_MASH`).

The `fitvd` extended classifier (`EXT_FITVD`) is based on a series of cuts in the space of measured size (`BDF_T`) versus signal-to-noise ($\log_{10}$(`BDF_S2N`); Figure A1). In this space, a set of precision-recall curves (i.e., completeness versus purity) were created by varying the `BDF_T` threshold to separate stars and galaxies. The cuts in this space were based on the threshold value that maximized the Matthews correlation coefficient, giving equal weights to stars and galaxies, and alternatives that gave higher weights to the purity of target populations. The threshold for each class is expressed as a linear interpolation function, f, that returns the threshold on `BDF_T` (y) as a function of $\log_{10}$(`BDF_S2N`) (x). The values for these interpolation functions are shown in Table A1. The integer value of the `EXT_FITVD` classifier is then defined as the sum of the thresholds that the object exceeds:

$$\mathtt{EXT\_FITVD} = \sum_{i}^{4} \{\mathrm{BDF_T} > f_i(\log_{10}(\mathrm{BDF_{S2N}}))\}. \tag{A1}$$

Table A1
Interpolation Nodes for `EXT_FITVD`

x	y_1	y_2	y_3	y_4
−3.0	−0.1	−0.028	0.028	0.252
0.79891862	−0.1	−0.028	0.028	0.252
0.90845217	−0.1	−0.028	0.008	0.188
0.98558583	−0.1	−0.028	0	0.14
1.05791208	−0.1	−0.028	0.004	0.096
1.13603715	−0.1	−0.028	0.012	0.104
1.22479487	−0.1	−0.028	0.012	0.052
1.33572223	−0.1	−0.012	0.004	0.048
1.48983602	−0.012	0.005	0.012	0.04
1.74124395	0.008	0.022	0.024	0.052
2.43187589	0.016	0.04	0.04	0.088
6.0	0.016	0.04	0.04	0.088

The weighted average extended classifier (`EXT_WAVG`) is built from the weighted average of the `SExtractor` *i*-band `SPREAD_MODEL` and `SPREADERR_MODEL` measurements from the individual exposures. This classifier makes use of the most accurate PSF for each individual exposure, but is limited

Table A2
Input Parameters to the `XGBoost` Star/Galaxy Classifier

Variable Name	Description
`CONC`	Concentration parameter from DESCONC
`BDF_T`	Multiepoch bulge + disk fit size parameter
$\log_{10}$(`BDF_S2N`)	Logarithm of the multiepoch bulge + disk fit signal-to-noise
`BDF_T_ERR`	Uncertainty on the multiepoch bulge + disk fit size parameter
`WAVG_SPREAD_MODEL_I`	weighted average `SExtractorSPREAD_MODEL` in the *i* band
`WAVG_SPREADERR_MODEL_I`	weighted average `SExtractorSPREADERR_MODEL` in the *i* band

to the depth of a single exposure:

$$\begin{aligned}\texttt{EXT\_WAVG} = {} & ((\texttt{WAVG\_SPREAD\_MODEL\_I} \\ & + 3.0{*}\texttt{WAVG\_SPREADERR\_MODEL\_I}) > 0.005) \\ & + ((\texttt{WAVG\_SPREAD\_MODEL\_I} \\ & + 1.0{*}\texttt{WAVG\_SPREADERR\_MODEL\_I}) > 0.003) \\ & + ((\texttt{WAVG\_SPREAD\_MODEL\_I} \\ & - 0.5{*}\texttt{WAVG\_SPREADERR\_MODEL\_I}) > 0.001).\end{aligned} \tag{A2}$$

The coadd extended classifier (`EXT_COADD`) is built from the `SExtractor` measurements of `SPREAD_MODEL` and `SPREADERR_MODEL` on the *i*-band coadd images. This is the most complete classifier (returning a value for nearly every object), but it suffers from the limitations of the coadded image PSF that is subject to discontinuities and sharp variations in depth. For this reason, it is given the lowest priority:

$$\begin{aligned}\texttt{EXT\_COADD} = {} & ((\texttt{SPREAD\_MODEL\_I} \\ & + 3.0{*}\texttt{SPREADERR\_MODEL\_I}) > 0.005) \\ & + ((\texttt{SPREAD\_MODEL\_I} \\ & + 1.0{*}\texttt{SPREADERR\_MODEL\_I}) > 0.003) \\ & + ((\texttt{SPREAD\_MODEL\_I} \\ & - 1.0{*}\texttt{SPREADERR\_MODEL\_I}) > 0.002).\end{aligned} \tag{A3}$$

The combined extended classifier, `EXT_MASH`, is assembled from the combination of `EXT_FITVD`, `EXT_WAVG`, and `EXT_COADD` classifications:

$$\texttt{EXT\_MASH} = \left\{\begin{array}{ll}\texttt{EXT\_FITVD}, & \text{if } \texttt{EXT\_FITVD} > -9 \\ \texttt{EXT\_WAVG}, & \text{elif } \texttt{EXT\_WAVG} > -9 \\ \texttt{EXT\_COADD}, & \text{elif } \texttt{EXT\_COADD} > -9 \\ -9, & \text{otherwise}\end{array}\right\}. \tag{A4}$$

A.2. `XGBoost` Classifier

Machine learning provides another well-tested approach to problems of star/galaxy classification (e.g., L. Cabayol et al. 2019). In the context of DES Y1, a wide variety of ML models were explored for star/galaxy classification (I. Sevilla-Noarbe et al. 2018). Here, we apply the popular gradient-boosted decision tree algorithm, `XGBoost` (T. Chen & C. Guestrin 2016), to perform a classification of stars and galaxies in DES Y6 Gold. Our training sample is assembled from two high-purity samples covering the bright and faint ends of the DES catalog. At the bright end, we use a combination of Gaia EDR3 morphology (Gaia Collaboration 2021) and SDSS DR17 spectral classifications (Abdurro'uf et al. 2022). At the faint end, we used the combination of HSC-SSP PDR2 morphology and CLAUDS infrared colors assembled in the XMM-LSS field by G. Desprez et al. (2023). In assembling these "truth" labels for training the `XGBoost` classifier, we were specifically focused on the purity of our samples rather than their completeness.

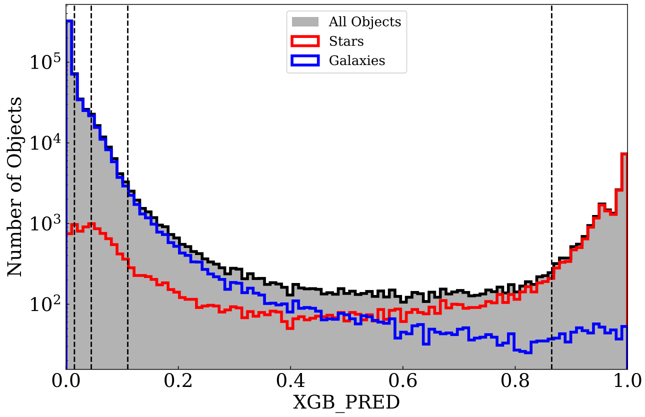

Figure A2. Performance of the `XGBoost` star/galaxy classifier output. The gray histogram represents the `XGB_PRED` value for all objects in a hold out test sample. The red histogram shows the distribution of objects with the truth label of stars, while the blue histogram shows distribution of objects with a truth label of galaxies. The dashed black lines show the thresholds used to define the `EXT_XGB` classes (4–0 from left to right).

The `XGBoost` model was trained on a set of six parameters listed in Table A2. During training, the input dataset was augmented with a small (5%) sample where one or more of the input parameters were explicitly set as missing. The `XGBoost` algorithm can deal with missing values through leaf trifurcation and was thus trained to be robust against one or more missing measurements in the real data. Optimization of the `XGBoost` hyperparameters was explored using scikit-learn `RandomSearchCV`. The specific scientific focus when designing the `XGBoost` classifier was on maximizing the completeness and purity of the *stellar* sample at faint magnitudes; however, it was also found to deliver excellent performance for galaxies.

The output of the `XGBoost` classifier is a continuous valued variable (`XGB_PRED`), for which an example distribution is shown in Figure A2. Values of `XGB_PRED` ~ 0 indicate extended (galaxy-like) objects, while values of `XGB_PRED` ~ 1 indicate pointlike (stellar) objects. Following the convention of the classical cut-based classifiers (Appendix A.1), the sample of objects was divided into discrete classes enumerated by integer values of $\{-9, 0, 1, 2, 3, 4\}$ by placing cuts on the `XGB_PRED` output. The placement of these cuts was designed to return approximately the same number of objects as the equivalent `EXT_MASH` class when applied to the full DES Y6 Gold object catalog. Again, a value of `EXT_XGB` $= -9$ indicates no data. In general, the `XGBoost`-based classifier is found to outperform the conventional classifiers (i.e., giving higher efficiency at fixed contamination, or vice versa, lower contamination at fixed efficiency). However, the `XGBoost` classification has not been implemented on simulation–injection–recovery tests due to the fact that the `CONC` parameter was not measured for the simulated object samples.

$$\begin{aligned} \texttt{EXT\_XGB} = {} & (\texttt{XGB\_PRED} < 0.865) \\ & + (\texttt{XGB\_PRED} < 0.110) \\ & + (\texttt{XGB\_PRED} < 0.045) \\ & + (\texttt{XGB\_PRED} < 0.015). \end{aligned} \tag{A5}$$

A.3. Classifier Performance

Table A3 summarizes the integrated performance of the conventional and `XGBoost` star/galaxy classifiers as a function of magnitude and object class. We provide these performance metrics for two different samples of objects: (1) a relatively bright sample ($17.5 < \texttt{MAG\_AUTO\_I} < 22.5$) that is intended as a proxy for the galaxy samples used for large-scale structure cosmology analyses, and (2) a more expansive sample similar to what might be considered for more general astronomical analyses ($16.5 < \texttt{MAG\_AUTO\_I} < 23.5$). A direct comparison between the conventional `EXT_MASH` and `XGBoost` classifiers is not possible from this table since the two algorithms classes are not matched on efficiency or contamination for this specific sample of objects. However, studies have found that the `XGBoost` classifier outperforms the `EXT_MASH` classifier when cuts on `XGB_PRED` are set to match the `EXT_MASH` classes on either efficiency (e.g., lower contamination at fixed efficiency) or contamination (e.g., higher efficiency at fixed contamination).

Table A3
Performance of the Morphological Star/Galaxy Separation

Selection	$17.5 \leqslant \texttt{MAG\_AUTO}_{\texttt{I}} \leqslant 22.5$		$16.5 \leqslant \texttt{MAG\_AUTO}_{\texttt{I}} \leqslant 23.5$	
	Efficiency	Contamination	Efficiency	Contamination
		Galaxy Selection		
$2 \leqslant \texttt{EXT\_MASH} \leqslant 4$	99.6%	1.3%	99.2%	1.8%
$3 \leqslant \texttt{EXT\_MASH} \leqslant 4$	99.6%	1.3%	98.8%	1.6%
$\texttt{EXT\_MASH} = 4$	98.6%	0.8%	96.3%	1.0%
$2 \leqslant \texttt{EXT\_XGB} \leqslant 4$	99.0%	0.5%	97.7%	1.0%
$3 \leqslant \texttt{EXT\_XGB} \leqslant 4$	98.3%	0.4%	96.2%	0.8%
$\texttt{EXT\_XGB} = 4$	96.7%	0.3%	92.5%	0.5%
$\texttt{XGB\_PRED} \leqslant 0.65$	99.6%	1.1%	99.5%	2.1%
$\texttt{XGB\_PRED} \leqslant 0.50$	99.6%	0.9%	99.3%	1.7%
$\texttt{XGB\_PRED} \leqslant 0.058$	98.6%	0.4%	96.7%	0.8%
		Stellar Selection		
$0 = \texttt{EXT\_MASH}$	89.2%	0.7%	80.0%	2.0%
$0 \leqslant \texttt{EXT\_MASH} \leqslant 1$	94.6%	1.5%	88.9%	5.2%
$0 \leqslant \texttt{EXT\_MASH} \leqslant 2$	94.7%	1.6%	90.2%	7.1%
$0 = \texttt{EXT\_XGB}$	92.1%	1.0%	79.3%	1.5%
$0 \leqslant \texttt{EXT\_XGB} \leqslant 1$	98.0%	4.0%	94.3%	12.5%
$0 \leqslant \texttt{EXT\_XGB} \leqslant 2$	98.5%	6.4%	95.6%	19.2%
$\texttt{XGB\_PRED} > 0.906$	89.2%	0.9%	74.8%	1.1%
$\texttt{XGB\_PRED} > 0.76$	94.6%	1.2%	84.2%	2.2%
$\texttt{XGB\_PRED} > 0.75$	94.7%	1.3%	84.6%	2.2%

Note. The `EXT_XGB` classes were assigned to give a similar number of objects per class as `EXT_MASH`. The `XGB_PRED` cuts were tuned to give the same completeness as `EXT_MASH` on the specific evaluation dataset used.

Appendix B
Main Catalog Columns

In Table B1 we summarize the essential columns of the Y6 Gold dataset with their brief description. Full details will be provided upon release at https://des.ncsa.illinois.edu/releases.

Table B1
Selected Y6 Gold Catalog Columns

Y6 Gold Catalog Column Family	Units	Description
COADD_OBJECT_ID	⋯	Unique identifier for a Y6 coadd object
TILENAME	⋯	Coadd tile to which the object belongs to. See E. Morganson et al. (2018)
RA, DEC, GLAT, GLON	deg	Equatorial and Galactic coordinates
ALPHAWIN_J2000, DELTAWIN_J2000	deg	Equatorial coordinates using a Gaussian-windowed measurement (for precise astrometry)
(BDF/GAP)_(MAG/FLUX)_(GRIZY)	magnitudes counts per second	Photometry as measured by the `fitvd` algorithm, both for bulge and disk model or a Gaussian aperture fit
PSF_(MAG/FLUX)_APER8_(GRIZY)	magnitudes counts per second	PSF photometry as measured by the `fitvd` algorithm, in APER8 system
(BDF/GAP)_(MAG/FLUX)_ERR_(GRIZY)	magnitudes counts per second	Estimated error for the BDF/GAP_(MAG/FLUX)
BDF_FLUX_COV_(1-5)_(1-5)	counts per second	Elements of the 5×5 flux covariance matrix for the BDF fit
PSF_(MAG/FLUX)_ERR_APER8_(GRIZY)	magnitudes counts per second	Estimated error to PSF_(MAG/FLUX)_APER8
(BDF/GAP)_(MAG/FLUX)_(GRIZY) _CORRECTED	magnitudes counts per second	FLUX corrected for interstellar extinction (i.e., dereddened; top of Galaxy) and PSF aperture ratio (APER8 system)
PSF_MAG_APER8_(GRIZY)_CORRECTED	mag	Magnitude measured by `fitvd` PSF model corrected for interstellar extinction (dereddened top of Galaxy) and PSF aperture ratio (APER8 system). Recommended for point-source studies
A_FIDUCIAL_(GRIZY)	mag	SED-independent interstellar extinction based on the $E(B - V)$ reddening map of D. J. Schlegel et al. (1998, SFD98)
BDF_T	arcsec^2	Intrinsic squared size of best-fit BDF model, before PSF convolution: $T = \langle x^2 \rangle + \langle y^2 \rangle$
BDF_T_ERR	arcsec^2	Estimate of error in BDF_T
BDF_T_RATIO	⋯	Ratio of BDF_T of the object to PSF_T at the location of the object (stars are near zero)
BDF_FRACDEV	⋯	Fraction of light in a bulge (Sérsic $n = 4$ model)
BDF_G_(1/2)	⋯	BDF ellipticity components
EXT_(COADD/FITVD/MASH/ WAVG/XGB)	⋯	Classification code for the "extendedness" of object, from 0 (pointlike) to 4 (extended-like). See Section 4.2
XGB_PRED	⋯	Predictor output from the XGBoost star/galaxy classifier. Galaxies have XGB_PRED $\sim$0 and stars have XGB_PRED $\sim$1. See Section 4.2
FLAGS_FOOTPRINT	⋯	Flag indicating that the object belongs to Y6 Gold. See Section 5.1
FLAGS_GOLD	⋯	Flag showing possible processing issues with the object. See Section 4.3
FLAGS_FOREGROUND	⋯	Flag showing that the object is in the area of influence of a foreground object from an imaging point of view. See Section 5.2
DNF_(Z/ZN)	⋯	DNF photo-z estimate for the object, using DNF_NNEIGHBORS or the nearest neighbor. See Section 4.4

Table B1
(Continued)

Y6 Gold Catalog Column Family	Units	Description
DNF_ZSIGMA	⋯	DNF photo-z uncertainty estimate from photometric uncertainties and residuals from the neighborhood fit
DNF_NNEIGHBORS	⋯	Number of neighbors used for the DNF_Z estimate
DNF_ZERR_PARAM	⋯	The uncertainty on DNF_Z due to photometric errors
DNF_ZERR_FIT	⋯	The uncertainty on DNF_Z from the residuals of the fit

Note. Names in parentheses show options for a given type of column separated by slashes for each column. Full details at https://des.ncsa.illinois.edu/releases.

Appendix C
Survey Property Maps

Survey property maps are computed from a base `mangle` polygon file and converted to `HEALPix` maps, as described in I. Sevilla-Noarbe et al. (2021).

In addition to these, certain survey property maps were also created using `decasu`, which is meant to be a complete replacement for `mangle` mapping, running a high-resolution pixelized map quickly and efficiently. This software natively uses `healsparse` formatted maps that are designed to store high-resolution information without dramatically increasing the memory usage (therefore allowing one to go beyond the limit of `nside` = 4096 imposed by standard RAM machine limitations). While `mangle` is better at describing the maps at the highest ("true") resolution, in practice we cannot make use of these maps without pixelizing and degrading them.

In Table C1 we summarize the observing conditions per band.

Figures C1 and C2 show two example maps as a function of position in the sky and the corresponding histogram of computed values for these positions (computed in `nside` = 4096 `HEALPix` resolution). Note that the linear features along equal R.A. values are a consequence of the observation strategy to ensure a complete tiling of the sphere.

C.1. Cirrus/Nebulosity Maps

Although the DES footprint avoids the Galactic plane, some regions are nonetheless affected by Galactic cirrus/nebulosity. These are being incorporated for the first time to the Gold suite of survey property maps with Y6 Gold.

Galactic cirrus manifests as faint diffuse light with surface brightness variations on scales between a few arcseconds and a few arcminutes. For comparison, background estimation using the AstrOmatic software (both `SExtractor` and `SWarp`) sampled a scale of 256 × 256 pixels ($\sim 67'' \times 67''$), and therefore, unaccounted structured diffuse light on smaller angular scales can impact object detection and measurements. To better understand the extent of cirrus light, and potentially provide a means to quantify or mitigate its impact on source detection and measurement, we investigated the use of an existing machine learning application, `MaxiMask`[83] (M. Paillassa et al. 2020), which was trained on individual DECam observations to identify a number of different characteristics, with nebular/diffuse light being the one of interest here. For faint diffuse light, we find that the default training provides a good discriminant for the presence of this nebulosity for the DES Y6 coadded images, and even spatially binned coadded images.

To obtain a map of nebular light across the DES footprint, we performed the following steps for each of the five DES bands for every DES coadd tile:

1. Start with the DES `coadd_nobkg` image products that were assembled by `SWarp` without applying a background subtraction (i.e., `-SUBTRACT_BACK N`).
2. Bin each coadd image by calculating the median of the values in groups of 5 × 5 pixels.
3. Run `MaxiMask` to obtain a probability-like estimate, ζ, for which the flux detected in each binned pixel is consistent with a diffuse/nebular origin.
4. Map each binned pixel onto `HEALPix` grids with `nside` = 1024 and 4096 (NESTED) and then accumulate statistics within each `HEALPix` element to form maps of median and maximum values of ζ, as well as the median and maximum surface brightness.

The resulting maps of max(ζ) in the *gri* bands show good correspondence to maps of extinction and to HI surveys when constrained to high velocities (i.e., Galactic cirrus). At longer wavelengths (zY bands), the detection of diffuse nebulosity is less significant, and the correspondence to the extinction and H I maps is less pronounced.

---

[83] This work used https://github.com/mpaillassa/MaxiMask/ version 1.0.

Table C1
Y6 Gold Survey Properties

DES Map Name (from `mangle`)[a]	Units	Description
NUMIMAGE	⋯	Number of images
MAGLIM	⋯	Magnitude limit estimated from the weight maps[b]
FRACDET	⋯	Fraction of the `HEALPix` pixel that has been observed (according to `mangle` geometry, using a subpixelization of 16 pixels per pixel) in each band and simultaneously in *grizY* and *griz*. This considers bleed-trail and bright star masks.
EXPTIME.SUM	s	Exposure time
T_EFF.(WMEAN/MAX/MIN)	⋯	Figure of merit for quality of observations t_{eff}[c]
T_EFF_EXPTIME.SUM	s	Exposure time multiplied by t_{eff}
SKYBRITE.WMEAN	electrons/CCD pixel	Sky brightness from the sky background model[d]
SKYVAR.(WMEAN/MIN/MAX)	(electrons/CCD pixel)^2	Variance on the sky brightness[e]
SKYVAR_SQRT.WMEAN	electrons/CCD pixel	Square root of sky variance
SKYVAR_UNCERTAINTY	electrons/s/coadd pixel	Sky variance with flux scaled by zero-point
SIGMA_MAG_ZERO.QSUM	mag	Quadrature sum of zero-point uncertainties
FWHM.(WMEAN/MIN/MAX)	arcsec	Average FWHM of the 2D elliptical Moffat function that best fits the PSF model from `PSFEx`
FWHM_FLUXRAD.(WMEAN/MIN/MAX)	arcsec	Twice the average half-light radius from the sources used for determining the PSF with `PSFEx`
FGCM_GRY.(WMEAN/MIN/MAX)	mag	Residual "gray" corrections to the zero-point from FGCM
AIRMASS.(WMEAN/MIN/MAX)	⋯	Secant of the zenith angle
CIRRUS_NEB_(MEAN/MAX)	⋯	Mean or maximum probability of nebular emission
CIRRUS_SB_(MEAN/MAX)	⋯	Mean surface brightness in image pixels (relative values)
DES map name (from `decasu`)[f]		
airmass_wmean	⋯	Secant of the zenith angle
fwhm_wmean	pixels	Average FWHM of the 2D elliptical Moffat function fit to the `PSFEx` model (0.263 arcsec pix^{-1})
maglim_wmean	mag	Magnitude limit estimated from the weight maps
nexp_sum	⋯	Number of exposures
exptime_sum	s	Exposure time
skybrite_wmean(_scaled) [g]	electrons/CCD pixel	Sky brightness from the sky background model
skysigma_wmean(_scaled) [g]	electrons/CCD pixel	Square root of sky variance
dcr_(dra/ddec/e1/e2)_wmean		Differential chromatic refraction effect on positions and ellipticity (relative shifts)
bdf_nside(4096/16,384)(_nodered)_depth	mag	Magnitude limit, using raw or dereddened magnitudes, in `nside` = 4096/16,384 `HEALPix` resolution

Notes. Survey properties in Y6 Gold registered as maps. Each quantity has been calculated individually for *grizY* bands.

[a] These maps are produced in `HEALPix` format in `nside` = 4096 in `NESTED` ordering, averaging from a higher-resolution version (`nside` = 32768). Each high-resolution pixel adopts the value of the molygon from the `mangle` map at its center, which is a statistic of a stack of images contributing to that point in the sky. `WMEAN` quantities are the mean value weighted using the weights obtained from `mangle`. `MIN`, `MAX` correspond to the minimum or maximum of all of the stacked images in the molygon. `SUM` adds up the contribution of all images to the molygon. `QSUM` makes a quadrature sum instead. The DES map name is the name given to the files as they are delivered in the release page.

[b] 10σ magnitude limit in $2''$ diameter apertures.

[c] t_{eff}, as described in E. Morganson et al. (2018), Equation (4), is measured as a ratio between exposure time and the exposure time necessary to achieve the same signal-to-noise for point sources observed in nominal conditions. This depends on a set of fiducial conditions per band for FWHM, sky background and atmospheric transmission.

[d] The model value used is taken as the median per CCD. Details for this model are described in G. M. Bernstein et al. (2017) and E. Morganson et al. (2018).

[e] Takes into account intrinsic sky Poisson noise, read noise and flat-field variance.

[f] These maps are produced in `healsparse` format, with weighted means unless indicated otherwise.

[g] Scaled quantities indicate that the electron/pixel values have been scaled according to the zero-points of the coadds.

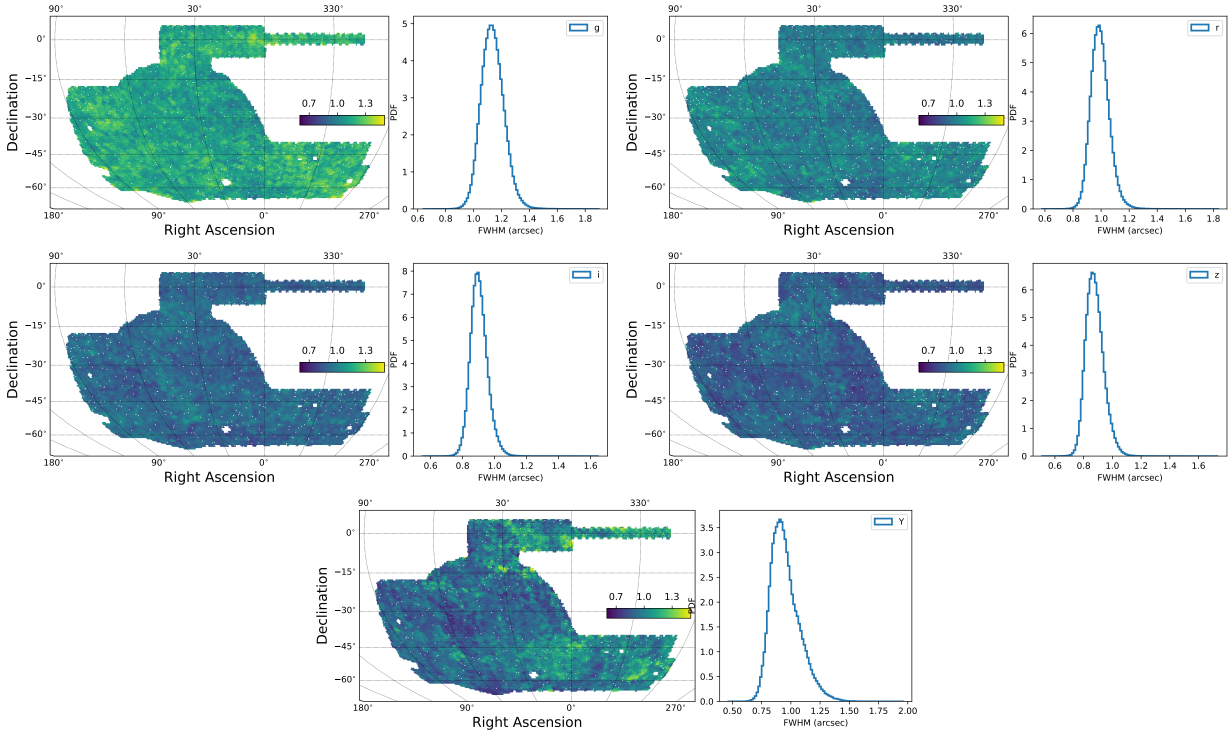

Figure C1. Sky maps and histograms of the seeing (fwhm_wmean) for each of the observed bands. The value at each location is the inverse-sky-variance-weighted sum of all individual exposures of that `HEALPix` pixel.

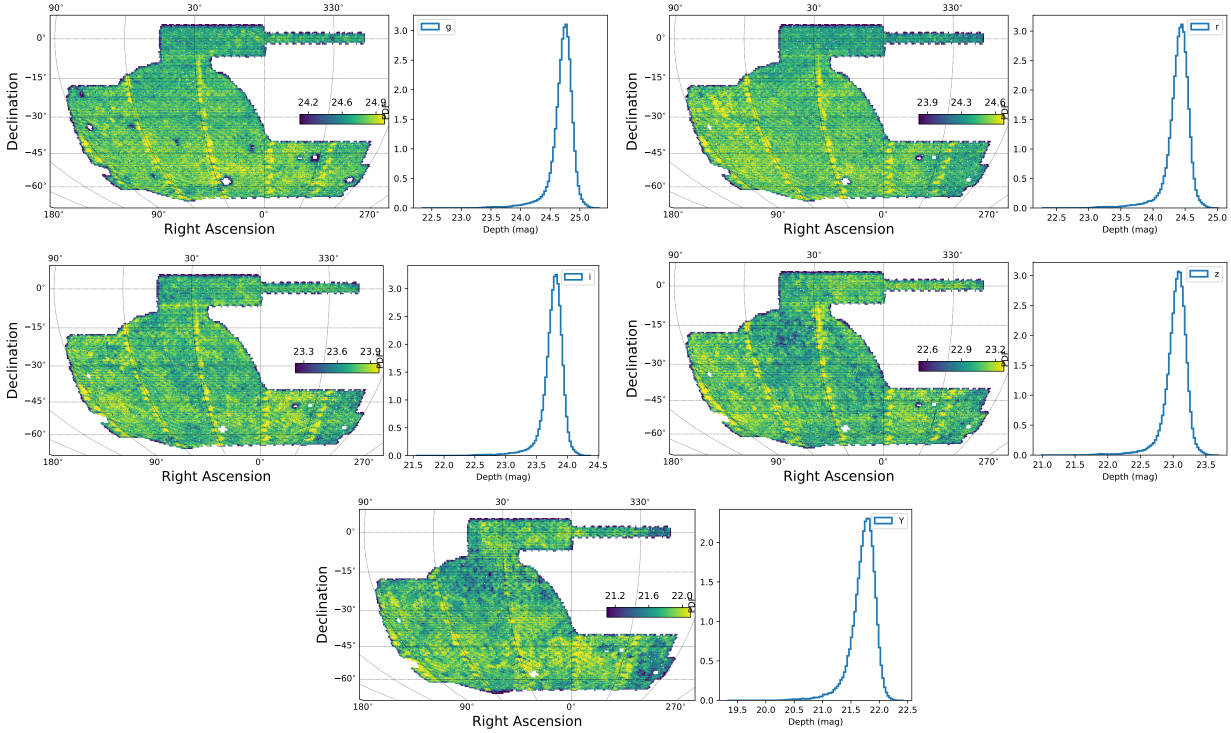

Figure C2. Sky maps and histograms for the magnitude limit (maglim_wmean) estimated from the weight maps. Note that the linear features along equal R.A. values are a result from regions covered by more than 10 exposures per band, which are inevitable when attempting to tile the sphere with no less than 10 exposures per location.

ORCID iDs

K. Bechtol https://orcid.org/0000-0001-8156-0429
I. Sevilla-Noarbe https://orcid.org/0000-0002-1831-1953
A. Drlica-Wagner https://orcid.org/0000-0001-8251-933X
B. Yanny https://orcid.org/0000-0002-9541-2678
R. A. Gruendl https://orcid.org/0000-0002-4588-6517
E. Sheldon https://orcid.org/0000-0001-9194-0441
E. S. Rykoff https://orcid.org/0000-0001-9376-3135
J. De Vicente https://orcid.org/0000-0001-8318-6813
M. Adamow https://orcid.org/0000-0002-6904-359X
D. Anbajagane https://orcid.org/0000-0003-3312-909X
M. R. Becker https://orcid.org/0000-0001-7774-2246
G. M. Bernstein https://orcid.org/0000-0002-8613-8259
A. Carnero Rosell https://orcid.org/0000-0003-3044-5150
J. Gschwend https://orcid.org/0000-0003-3023-8362
M. Gorsuch https://orcid.org/0000-0002-3135-3824
W. G. Hartley https://orcid.org/0000-0001-9994-1115
M. Jarvis https://orcid.org/0000-0002-4179-5175
T. Jeltema https://orcid.org/0000-0001-6089-0365
R. Kron https://orcid.org/0000-0003-2643-7924
T. A. Manning https://orcid.org/0000-0003-2545-9195
J. O'Donnell https://orcid.org/0000-0003-4083-1530
A. Pieres https://orcid.org/0000-0001-9186-6042
M. Rodríguez-Monroy https://orcid.org/0000-0001-6163-1058
D. Sanchez Cid https://orcid.org/0000-0003-3054-7907
M. Tabbutt https://orcid.org/0000-0002-0690-1737
C. Y. Tan https://orcid.org/0000-0003-0478-0473
L. Toribio San Cipriano https://orcid.org/0000-0002-8313-7875
D. L. Tucker https://orcid.org/0000-0001-7211-5729
N. Weaverdyck https://orcid.org/0000-0001-9382-5199
M. Yamamoto https://orcid.org/0000-0003-1585-997X
T. M. C. Abbott https://orcid.org/0000-0003-1587-3931
M. Aguena https://orcid.org/0000-0001-5679-6747
A. Alarcón https://orcid.org/0000-0001-8505-1269
S. Allam https://orcid.org/0000-0002-7069-7857
A. Amon https://orcid.org/0000-0002-6445-0559
F. Andrade-Oliveira https://orcid.org/0000-0003-0171-6900
S. Avila https://orcid.org/0000-0001-5043-3662
P. H. Bernardinelli https://orcid.org/0000-0003-0743-9422
E. Bertin https://orcid.org/0000-0002-3602-3664
J. Blazek https://orcid.org/0000-0002-4687-4657
D. Brooks https://orcid.org/0000-0002-8458-5047
D. L. Burke https://orcid.org/0000-0003-1866-1950
J. Carretero https://orcid.org/0000-0002-3130-0204
F. J. Castander https://orcid.org/0000-0001-7316-4573
R. Cawthon https://orcid.org/0000-0003-2965-6786
C. Chang https://orcid.org/0000-0002-7887-0896
A. Choi https://orcid.org/0000-0002-5636-233X
C. Conselice https://orcid.org/0000-0003-1949-7638
M. Costanzi https://orcid.org/0000-0001-8158-1449
M. Crocce https://orcid.org/0000-0002-9745-6228
L. N. da Costa https://orcid.org/0000-0002-7731-277X
T. M. Davis https://orcid.org/0000-0002-4213-8783
S. Desai https://orcid.org/0000-0002-0466-3288
H. T. Diehl https://orcid.org/0000-0002-8357-7467
S. Dodelson https://orcid.org/0000-0002-8446-3859
P. Doel https://orcid.org/0000-0002-6397-4457
C. Doux https://orcid.org/0000-0003-4480-0096
A. Ferté https://orcid.org/0000-0003-3065-9941
B. Flaugher https://orcid.org/0000-0002-2367-5049
P. Fosalba https://orcid.org/0000-0002-1510-5214
J. Frieman https://orcid.org/0000-0003-4079-3263
J. García-Bellido https://orcid.org/0000-0002-9370-8360
M. Gatti https://orcid.org/0000-0001-6134-8797
E. Gaztanaga https://orcid.org/0000-0001-9632-0815
G. Giannini https://orcid.org/0000-0002-3730-1750
D. Gruen https://orcid.org/0000-0003-3270-7644
G. Gutierrez https://orcid.org/0000-0003-0825-0517
K. Herner https://orcid.org/0000-0001-6718-2978
S. R. Hinton https://orcid.org/0000-0003-2071-9349
D. L. Hollowood https://orcid.org/0000-0002-9369-4157
K. Honscheid https://orcid.org/0000-0002-6550-2023
D. Huterer https://orcid.org/0000-0001-6558-0112
N. Jeffrey https://orcid.org/0000-0003-2927-1800
E. Krause https://orcid.org/0000-0001-8356-2014
K. Kuehn https://orcid.org/0000-0003-0120-0808
O. Lahav https://orcid.org/0000-0002-1134-9035
S. Lee https://orcid.org/0000-0002-8289-740X
C. Lidman https://orcid.org/0000-0003-1731-0497
M. Lima https://orcid.org/0000-0002-4719-3781
H. Lin https://orcid.org/0000-0002-7825-3206
J. L. Marshall https://orcid.org/0000-0003-0710-9474
J. Mena-Fernández https://orcid.org/0000-0001-9497-7266
R. Miquel https://orcid.org/0000-0002-6610-4836
J. J. Mohr https://orcid.org/0000-0002-6875-2087
J. Muir https://orcid.org/0000-0002-7579-770X
J. Myles https://orcid.org/0000-0001-6145-5859
R. L. C. Ogando https://orcid.org/0000-0003-2120-1154
A. Palmese https://orcid.org/0000-0002-6011-0530
A. A. Plazas Malagón https://orcid.org/0000-0002-2598-0514
A. Porredon https://orcid.org/0000-0002-2762-2024
J. Prat https://orcid.org/0000-0002-5933-5150
M. Raveri https://orcid.org/0000-0002-7354-3802
A. K. Romer https://orcid.org/0000-0002-9328-879X
A. Roodman https://orcid.org/0000-0001-5326-3486
S. Samuroff https://orcid.org/0000-0001-7147-8843
E. Sanchez https://orcid.org/0000-0002-9646-8198
M. Smith https://orcid.org/0000-0002-3321-1432
M. Soares-Santos https://orcid.org/0000-0001-6082-8529
E. Suchyta https://orcid.org/0000-0002-7047-9358
G. Tarle https://orcid.org/0000-0003-1704-0781
M. A. Troxel https://orcid.org/0000-0002-5622-5212
A. R. Walker https://orcid.org/0000-0002-7123-8943
J. Weller https://orcid.org/0000-0002-8282-2010
P. Wiseman https://orcid.org/0000-0002-3073-1512
Y. Zhang https://orcid.org/0000-0001-5969-4631

References

Abazajian, K. N., Adelman-McCarthy, J. K., Agüeros, M. A., et al. 2009, ApJS, 182, 543
Abbott, T. M. C., Alarcon, A., Allam, S., et al. 2019, PhRvL, 122, 171301
Abdurro'uf, Accetta, K., Aerts, C., et al. 2022, ApJS, 259, 35
Ahumada, R., Allende Prieto, C., Almeida, A., et al. 2020, ApJS, 249, 3
Aihara, H., AlSayyad, Y., Ando, M., et al. 2019, PASJ, 71, 114
Aihara, H., AlSayyad, Y., Ando, M., et al. 2022, PASJ, 74, 247
Alam, S., Aubert, M., Avila, S., et al. 2021, PhRvD, 103, 083533
Anbajagane, D., Tabbutt, M., Beas-Gonzalez, J., et al. 2025, OJAp, 8, 65
Astropy Collaboration 2013, A&A, 558, A33
Baldry, I. K., Robotham, A. S. G., Hill, D. T., et al. 2010, MNRAS, 404, 86
Bernstein, G. M., Abbott, T. M. C., Desai, S., et al. 2017, PASP, 129, 114502
Bernstein, G. M., & Armstrong, R. 2014, MNRAS, 438, 1880
Bertin, E. 2006, ASPC, 351, 112

Bertin, E., 2010 SWarp: Resampling and Co-adding FITS Images Together, Astrophysics Source Code Library, ascl:1010.068
Bertin, E. 2011, ASPC, 442, 435
Bertin, E., & Arnouts, S. 1996, A&AS, 117, 393
Bertin, E., Mellier, Y., Radovich, M., et al. 2002, ASPC, 281, 228
Bosch, J., AlSayyad, Y., Armstrong, R., et al. 2019, ASPC, 523, 521
Bosch, J., Armstrong, R., Bickerton, S., et al. 2018, PASJ, 70, S5
Brout, D., Sako, M., Scolnic, D., et al. 2019, ApJ, 874, 106
Burke, D. L., Rykoff, E. S., Allam, S., et al. 2018, AJ, 155, 41
Cabayol, L., Sevilla-Noarbe, I., Fernández, E., et al. 2019, MNRAS, 483, 529
Carlstrom, J. E., Ade, P. A. R., Aird, K. A., et al. 2011, PASP, 123, 568
Carrasco Kind, M., Drlica-Wagner, A., Koziol, A., & Petravick, D. 2019, JOSS, 4, 1022
Chambers, K. C., Magnier, E. A., Metcalfe, N., et al. 2016, arXiv:1612.05560
Chen, T., & Guestrin, C. 2016, in Proc. of the 22nd ACM SIGKDD Int. Conf. on Knowledge Discovery and Data Mining, ed. B. Krishnapuram et al. (Association of Computing Machinery), 785
Colless, M., Peterson, B. A., Jackson, C., et al. 2003, arXiv:0306581
De Vicente, J., Sánchez, E., & Sevilla-Noarbe, I. 2016, MNRAS, 459, 3078
DES Collaboration 2005, arXiv:0510346
DES Collaboration 2016, MNRAS, 460, 1270
DESI Collaboration 2016, arXiv:1611.00036
DES Collaboration 2018, ApJS, 239, 18
DES Collaboration 2021, ApJS, 255, 20
DES Collaboration 2022, PhRvD, 105, 023520
DES Collaboration 2024a, PhRvD, 110, 063515
DES Collaboration 2024b, ApJL, 973, L14
DES Collaboration 2025, JCAP, 2025, 012
Desprez, G., Picouet, V., Moutard, T., et al. 2023, A&A, 670, A82
Dey, A., Schlegel, D. J., Lang, D., et al. 2019, AJ, 157, 168
Drlica-Wagner, A., Carlin, J. L., Nidever, D. L., et al. 2021, ApJS, 256, 2
Drlica-Wagner, A., Sevilla-Noarbe, I., Rykoff, E. S., et al. 2018, ApJS, 235, 33
Euclid Collaboration 2025, A&A, 697, A1
Everett, S., Yanny, B., Kuropatkin, N., et al. 2022, ApJS, 258, 15
Flaugher, B., Diehl, H. T., Honscheid, K., et al. 2015, AJ, 150, 150
Gaia Collaboration 2016, A&A, 595, A2
Gaia Collaboration 2018, A&A, 616, A14
Gaia Collaboration 2021, A&A, 649, A1
Gaia Collaboration 2023, A&A, 674, A1
Giannini, G., Alarcon, A., Gatti, M., et al. 2024, MNRAS, 527, 2010
Górski, K. M., Hivon, E., Banday, A. J., et al. 2005, ApJ, 622, 759
Gschwend, J., Rossel, A. C., Ogando, R. L. C., et al. 2018, A&C, 25, 58
Gwyn, S., McConnachie, A. W., Cuillandre, J.-C., et al. 2025, AJ, 170, 324
Hamilton, A. J. S., & Tegmark, M. 2004, MNRAS, 349, 115
Hartley, W. G., Chang, C., Samani, S., et al. 2020, MNRAS, 496, 4769
Hartley, W. G., Choi, A., Amon, A., et al. 2022, MNRAS, 509, 3547
Heymans, C., Tröster, T., Asgari, M., et al. 2021, A&A, 646, A140
Hoffleit, D., & Jaschek, C. 1991, The Bright Star Catalogue (5th ed.; Yale Univ. Observatory)
Hunter, J. D. 2007, CSE, 9, 90
Ivezić, Ž., Kahn, S. M., Tyson, J. A., et al. 2019, ApJ, 873, 111
Jarvis, M., Bernstein, G. M., Amon, A., et al. 2021, MNRAS, 501, 1282
Jarvis, M., Sheldon, E., Zuntz, J., et al. 2016, MNRAS, 460, 2245
Kuijken, K., Heymans, C., Dvornik, A., et al. 2019, A&A, 625, A2
Le Fèvre, O., Cassata, P., Cucciati, O., et al. 2013, A&A, 559, A14
Lidman, C., Tucker, B. E., Davis, T. M., et al. 2020, MNRAS, 496, 19
Makarov, D., Prugniel, P., Terekhova, N., Courtois, H., & Vauglin, I. 2014, A&A, 570, A13
McBryde, F. W., & Thomas, P. 1949, Equal-area Projections for World Statistical Maps (U.S. Government Printing Office), 245, https://library.oarcloud.noaa.gov/docs.lib/htdocs/rescue/cgs_specpubs/QB275U35no2451949.pdf
McMahon, R. G., Banerji, M., Gonzalez, E., et al. 2013, Msngr, 154, 35
Morganson, E., Gruendl, R. A., Menanteau, F., et al. 2018, PASP, 130, 074501
Myles, J., Alarcon, A., Amon, A., et al. 2021, MNRAS, 505, 4249
Neilsen, E. H., Annis, J. T., Diehl, H. T., et al. 2019, arXiv:1912.06254
Newman, J. A., Cooper, M. C., Davis, M., et al. 2013, ApJS, 208, 5
Paillassa, M., Bertin, E., & Bouy, H. 2020, A&A, 634, A48
Pence, W. D., White, R. L., & Seaman, R. 2010, PASP, 122, 1065
Planck Collaboration 2020, A&A, 641, A6
Rodríguez-Monroy, M., Weaverdyck, N., Elvin-Poole, J., et al. 2022, MNRAS, 511, 2665
Rozo, E., Rykoff, E. S., Abate, A., et al. 2016, MNRAS, 461, 1431
Rykoff, E. S., Tucker, D. L., Burke, D. L., et al. 2023, arXiv:2305.01695
Schlafly, E. F., & Finkbeiner, D. P. 2011, ApJ, 737, 103
Schlafly, E. F., Finkbeiner, D. P., Schlegel, D. J., et al. 2010, ApJ, 725, 1175
Schlegel, D. J., Finkbeiner, D. P., & Davis, M. 1998, ApJ, 500, 525
Scodeggio, M., Guzzo, L., Garilli, B., et al. 2018, A&A, 609, A84
Sevilla-Noarbe, I., Hoyle, B., Marchã, M. J., et al. 2018, MNRAS, 481, 5451
Sevilla-Noarbe, I., Bechtol, K., Carrasco Kind, M., et al. 2021, ApJS, 254, 24
Sheldon, E. S. 2014, MNRAS, 444, L25
Sheldon, E. S., Becker, M. R., Jarvis, M., Armstrong, R. & LSST Dark Energy Science Collaboration 2023, OJAp, 6, 17
Sheldon, E. S., Becker, M. R., MacCrann, N., & Jarvis, M. 2020, ApJ, 902, 138
Skrutskie, M. F., Cutri, R. M., Stiening, R., et al. 2006, AJ, 131, 1163
Smith, M., D'Andrea, C. B., Sullivan, M., et al. 2020, AJ, 160, 267
Spergel, D., Gehrels, N., Baltay, C., et al. 2015, arXiv:1503.03757
Swanson, M. E. C., Tegmark, M., Hamilton, A. J. S., & Hill, J. C. 2008, MNRAS, 387, 1391
Taylor, M. B. 2005, ASPC, 347, 29
Toribio San Cipriano, L., De Vicente, J., Sevilla-Noarbe, I., et al. 2024, A&A, 686, A38
van den Busch, J. L., Hildebrandt, H., Wright, A. H., et al. 2020, A&A, 642, A200
Van Der Walt, S., Colbert, S. C., & Varoquaux, G. 2011, CSE, 13, 22
Virtanen, P., Gommers, R., Oliphant, T. E., et al. 2020, NatMe, 17, 261
Weaverdyck, N., Rodríguez-Monroy, M., Elvin-Poole, et al. 2026, arXiv:2601.14484
Yamamoto, M., Becker, M. R., Sheldon, E., et al. 2025, MNRAS, 543, 4156
Zonca, A., Singer, L., Lenz, D., et al. 2019, JOSS, 4, 1298